

NASA
Technical
Paper 211852

November 2002

**DISTRIBUTION OF BLADE-ELEMENT
STOCHASTIC TURBULENCE**

R. E. MCFARLAND

NASA, AMES Research Center

Moffett Field, CA 94035-1000 USA



National Aeronautics and
Space Administration

CONTENTS

SUMMARY	1
INTRODUCTION	1
THE THEORY	2
THE GEOMETRY	4
THE DISTRIBUTION ALGORITHM	6
CORRELATION	7
THE ROTOR SYSTEM	8
THE CENTER OF MASS	9
THE TAIL	9
TURBULENCE FILTERS	10
BANDWIDTH CONSIDERATIONS	13
NOISE SOURCE CONSIDERATIONS	15
PERFORMANCE	16
FREQUENCY FOLDING	17
CONCLUSIONS	18
REFERENCES	19
APPENDIX A: FILTER VELOCITIES	20
<i>Baseline Velocities</i>	<i>20</i>
<i>DOBEST Velocities</i>	<i>21</i>
APPENDIX B: TURBULENCE RESPONSES	23
APPENDIX C: REAL-TIME COMPUTATIONS	26
<i>Slowly Varying Functions</i>	<i>26</i>
<i>Fast Functions</i>	<i>27</i>

SYMBOLS

d_m	<i>normalized element distances (r_m/L)</i>
h (ft)	<i>vehicle altitude</i>
L (ft)	<i>turbulence characteristic length in x-y plane (L_u and L_v)</i>
L_w (ft)	<i>turbulence characteristic length in vertical axis</i>
m	<i>segment number</i>
$M_{n,m}$	<i>generalized roll axis torque produced by the vertical velocity at element r_m</i>
$[M]_m$	<i>matrix of correlation coefficients for radius r_m</i>
n	<i>blade number</i>
N	<i>number of blades</i>
p_m (rad/sec)	<i>filter pole at element r_m</i>
R_G (ft)	<i>distance from the hub to the tail rotor</i>
r_m (ft)	<i>m^{th} element's radius from the hub</i>
R_T (ft)	<i>rotor radius</i>
S_m	<i>series summation for average velocity computation at r_m</i>
$[T]$	<i>rotation matrix</i>
V_m (ft/sec)	<i>DOBEST model aerodynamic velocity of all elements at radius r_m</i>
$V_{n,m}$ (ft/sec)	<i>baseline model aerodynamic velocity of element (n,m)</i>
V_{RW} (ft/sec)	<i>vehicle aerodynamic velocity</i>
α_m	<i>equivalent discrete filter pole at element r_m</i>
$\alpha_{n,m}$, $\beta_{n,m}$	<i>element angles of attack and sideslip</i>
ε_i	<i>independent, random Gaussian variables, four per axis (12 total)</i>
μ_i	<i>rotated random variables, six per axis</i>
η_i	<i>random variables at all aerodynamic centers (22 per axis)</i>
ρ_m	<i>correlation coefficients between random variables separated by d_m</i>
ψ_n (rad)	<i>azimuth angle of the n^{th} blade</i>
Ω_T (rad/sec)	<i>main rotor angular velocity</i>
σ (ft/sec)	<i>turbulence dispersion in the x-y plane</i>
σ_w (ft/sec)	<i>turbulence dispersion in the vertical axis</i>
ω (rad/sec)	<i>temporal frequency</i>
Ω (rad/ft)	<i>spatial frequency</i>

DISTRIBUTION OF BLADE-ELEMENT STOCHASTIC TURBULENCE

R. E. McFarland

Ames Research Center

SUMMARY

A turbulence model applicable to a rotorcraft's complete flight envelope has been developed for real-time simulation. Invariant statistical properties are produced in each dimension by use of a novel interpolation algorithm for both rotating blade elements and fixed aerodynamic centers. The turbulence velocities at all locations are therefore statistically correlated as functions of relative position and turbulence scale lengths.

Invariant statistical properties are important for the specification of a uniform turbulent energy field for each axis. Correlation is important for the distribution of the field over the rotorcraft's geometry. The distribution of turbulence to aerodynamic centers induces moments, and obviates the rotational filters that are required in non-distributed aircraft models. The algorithm used to distribute turbulence over the rotor system includes blade rotation, while avoiding the intractable problem presented by cyclostationary filters.

Unlike previous turbulence models that require significant airspeed, low-speed and hovering operations are accommodated, where the turbulence scale length usually approaches that of the rotor diameter. In this case, variations in correlation over the rotor system become especially significant in generating the vehicle's rotational response to atmospheric disturbances.

INTRODUCTION

For many years the simulation community has used the military specification turbulence filters described in reference 1 in applications involving conventional aircraft models. For rotorcraft models, however, these filters present an unusual challenge. In particular, for sophisticated blade-element models such as the Black Hawk (UH-60) model of reference 2, the challenge is exemplified by the nonlinear behavior of the velocities of the individual blade elements. The spectral

representation of turbulence assumes stationary (or "slowly varying") coefficients, where these coefficients are functions of airspeed. From reference 1: "*The frozen field concept (Taylor's hypothesis) ... implies, in the frequency domain, that the temporal frequency ω (rad/sec) sensed by the airplane is related to the spatial frequency by the true airspeed V ; that is, $\omega = \Omega V$. Therefore the spectral densities are transformed to functions of ω as follows:*

$$\phi(\omega) = \frac{1}{V} \Phi\left(\Omega = \frac{\omega}{V}\right).$$

The mathematical destinations of this transformation are the coefficients of turbulence filters. These filters produce velocity components from Gaussian inputs. The purpose of the filters is twofold. They produce an integrated power spectral density that is given by the variance σ^2 , and for the Dryden turbulence model, they shape the spectral form by imposing a first-order high-frequency asymptote. Translational turbulence filters are typically represented in Laplace notation:

$$f(s) = \frac{\sigma \sqrt{3p/\pi} (s + p/\sqrt{3})}{(s + p)^2}$$

The quantity $p = V/L$ is referred to herein as the "pole"; L is the characteristic scale length of turbulence in a particular dimension, the inverse of which is sometimes referred to as the "wave number." Applying this filter to an element on a blade, the notation $V = V_{n,m}$ is used, where n is the blade number and m is the element number.

The cyclic behavior of element velocities in a rotor system presents an intractable problem to the discipline of simulation, unless a new approach is taken to turbulence simulation. A turbulence model is here derived called DOBEST (an acronym for the title of this paper), and this model is shown to create realistic turbulence velocities by applying mathematical algorithms amenable to real-time simulation. The effect of these algorithms is compared with a baseline model, which is determined to be inappropriate for simulation.

This baseline model uses a thorough description of the aerodynamic velocity at each blade-element location.

In the DOBEST model, average velocities are developed, as shown in appendix A. The filter coefficients for any radial station (on a “ring”) are then stationary for a given vehicle airspeed and altitude, eliminating the cyclostationary problem of the baseline model.

Body-axis disturbances utilize the vehicle’s aerodynamic velocity $V = V_{RW}$, and their filters are applied at the distributed aerodynamic centers of the vehicle. Hence, these components are similar to those used in turbulence for conventional aircraft simulations.

A complete baseline model, as well as the DOBEST model, is developed here. Although the baseline model contains an accurate representation of rotary dynamics, it produces divergent responses and meaningless energy metrics because of its cyclostationary filter coefficients. The DOBEST model does not have these problems.

Rotational turbulence filters are also used in turbulence models for conventional aircraft. However, in a distributed aircraft model, rotational responses are induced from position-dependent forces created by function evaluations using distributed aerodynamic velocities, including superimposed turbulence. Filters approximating rotational vehicle responses to turbulence are thus superfluous in a distributed model.

THE THEORY

Considering just a rotor system, turbulence filters model atmospheric disturbances, and these disturbances are superimposed upon the more profoundly developed physics of the rotating blades. In particular, airspeed differences on the advancing and retreating blades are accounted for in a blade-element rotor model such as that of reference 2. Since the filters are only spectral representations of turbulence, they do not have to be formulated as complete aerodynamic representations of blade activity, especially when such a formulation requires assumptions that invalidate the fundamental characteristic of the filters: outputs from *linear* filters excited by Gaussian noise remain Gaussian. This is not true when the filter coefficients are periodic functions of time. Such filters are “cyclostationary,” and are nonlinear functions of time. The effect of cyclostationary filters is illustrated herein by use of a baseline model, where it is shown that it is not possible to establish meaningful energy metrics for the turbulent field.

Consider the velocity of a blade-element located at a fixed radius r_m from the hub, where the blades rotate with an angular velocity given by Ω_T . The azimuth angle of a blade is given by

$$\psi_n = \int \Omega_T dt + 2\pi \left(\frac{n-1}{N} \right)$$

This angle is measured from the aft centerline of the vehicle, and N is the number of blades. Nominally, the rotor’s rpm is given by $\Omega_T = 27 \text{ rad/sec} = 4.3 \text{ Hz}$ for the Black Hawk model discussed herein, so that an element (n,m) velocity nominally has the frequency of 4.3 Hz.

As shown in appendix A, by including both the aircraft and rotational velocity components with respect to the mean wind, the aerodynamic velocity for an element located at r_m on the n^{th} blade is given by

$$V_{n,m} = \sqrt{V_{RW}^2 + \Omega_T^2 r_m^2 + 2\Omega_T r_m V_{RW} \cos\alpha \sin(\psi_n + \beta)}$$

This cyclic velocity, which may periodically vanish for an element whenever $\Omega_T r_m \approx V_{RW}$, is the component that produces cyclostationary filters, despite the fact that the rotational component $\Omega_T r_m$ is quite large at all element stations. The element velocity $V_{n,m}$, with its two subscripts representing blade number “ n ” and element number “ m ,” is that used in the baseline model.

The total element velocities, including flapping and lagging, are used in the rotor model to produce the angles of sideslip “ $\beta_{n,m}$ ” and attack “ $\alpha_{n,m}$ ” of the individual blade elements. Extensive mathematical operations, including multivariate function evaluations, accommodate nonlinear phenomena such as reverse flow on retreating blades (ref. 2). Considering the assumed linear form for turbulence filters, however, it is inconsistent to compute these gross, nonlinear velocities in the rotor system, and to then add incremental turbulence values that are themselves functions of the total nonlinear velocities. The filters assume stationary (or “slowly varying”) coefficients, and are only applicable for appreciable, positive velocities.

“The implication of [Taylor’s] hypothesis is that the turbulence-induced responses of the airplane result only from the motion of the airplane relative to the turbulent field. Experience has shown that the frozen field concept is entirely acceptable for those cases in which the mean wind velocity and the root-mean-square turbulence velocity are small relative to the ground speed of the airplane.” (ref. 1).

Hence, only appreciable velocities are accommodated by filters using Taylor's hypothesis, and regions around reverse flow on a blade are certainly precluded.

A design objective of the DOBEST model is to retain the military specification linear filters of reference 1, which deliver the required variance and first-order roll-off. Considering the above quote, the frozen-field concept becomes more valid by including the large rotational contributions in the velocity of each element. Indeed, the velocity then becomes so large that a discrete implementation of the filters indicates that an upper limit be imposed on the system pole ($p = V/L$) for computational accuracy. This phenomenon is related to the Nyquist criterion. Using realistic cycle times, accuracy could degrade at high flight speeds during low altitude flight, unless the turbulence scale length in the vertical dimension is restricted to a minimum value.

The DOBEST model is a new approach to simulating rotorcraft turbulence. A novel technique is used to distribute Gaussian noise to the geometrical locations of aerodynamic centers, including five elements located on each of four blades. These properly correlated values are then input to linear filters. The filter outputs retain the Gaussian characteristics of the inputs, and properly produce statistical correlation as a function of blade translation and rotation through a turbulent field. The DOBEST model is also designed to be very accurate when the magnitude of the scale length approaches that of the rotor diameter. This occurs for low-altitude flight.

The nonlinear rotor model (ref. 2) includes all of the cyclic dynamics, so the redundant inclusion of these dynamics in the creation of the incremental turbulence terms is not used in the DOBEST model. The baseline model, however, includes these cyclic dynamics and produces outputs that diverge. This phenomenon is shown in appendix B.

Magnitude arguments exist for not including cyclostationary phenomena in the turbulence contributions to a rotorcraft model. If the airspeed is large, turbulence increments to the rotor system represent minor contributions to the gross cyclic velocities, and vast computational power need not be dedicated to improving the accuracy of superimposed stochastic variables, which are highly correlated. If the vehicle's airspeed is small, the increments are computed quite accurately without the inclusion of cyclostationary dynamics (as in the DOBEST model), and their contribution to rotorcraft responses becomes more important. This occurs because the correlation between the individual elements is then small, owing to

small values of characteristic length (L). Low correlation can produce large rotational activity.

For the rotor's turbulence filters the DOBEST model uses the average element velocities, as developed in appendix A. There is considerable precedence for this operation in the field of turbulence modeling:

"...special consideration should be given to the anisotropic and nonhomogeneous nature of the turbulence. One way to sidestep this difficulty is to use average values of the turbulence model parameters..." (ref. 1).

Aerodynamic effects owing to velocity differences on advancing and retreating blades are otherwise handled in the blade-element model, and only stochastic disturbances are considered (not "discrete gusts"). The rotor's filter coefficients thus remain stationary (*i.e.*, "slowly varying"), because the turbulence filters for all elements at a given radius from the hub utilize an average aerodynamic velocity (single subscript) given by

$$V_m = \left(1 - S_m\right) \sqrt{V_{RW}^2 + \Omega_T^2 r_m^2 + 2\Omega_T r_m V_{RW} \cos\alpha}$$

where S_m is a series developed in appendix A. This formulation invariably produces large velocities ($V_m > 212$ ft/sec) in the rotor model's turbulence filter coefficients, independent of the direction of the mean wind. It also decreases the computational workload considerably, which nonetheless remains large, and avoids the cyclostationary dynamics that invalidate Gaussian assumptions. This invalidation for the baseline model is illustrated in appendix B.

For body-fixed aerodynamic centers, the conventional implementation of turbulence is used. These filters utilize the true airspeed (V_{RW}) of the vehicle, while inputs are distributed to aerodynamic centers.

Great care is taken here to preserve the Gaussian characteristics of stochastic turbulence, and thus retain realistic metrics for the energy in the turbulent field. A novel interpolation algorithm is introduced that retains the turbulence variance in each axis of the rotorcraft, while producing the proper covariances between aerodynamic centers. If required, nonlinear variations in the energy field, such as patchy turbulence, may be included in the dispersion coefficients.

The linear filter representation degrades for small aerodynamic velocities, because the filter's pole, zero, and gain vanish. This results in low-gain integration, and is shown to cause havoc in the baseline model.

Nonetheless, turbulence occurs in real flight despite low vehicle velocity with respect to the mean wind, and is a very important phenomenon in modeling rotorcraft operations at low altitudes. Use of the average velocity at each element station avoids this problem in the DOBEST model.

Especially for the vertical scale length L_w (as cited later), near sea level the turbulence wavelength approaches that of a typical rotor diameter, and in generating rotational disturbances the accompanying reduction in cross correlation is shown to be very important. Conversely, for high-altitude flight, where vehicle velocity is usually large, the characteristic scale length of turbulence is also large, such that the filter's pole (V/L) remains reasonable. A large turbulence scale length (or altitude) is shown to produce a high degree of correlation throughout the rotor system.

The theory may be summarized as follows: The proper distribution of Gaussian random variables throughout the rotor system is the dominating consideration in creating a representative simulation of rotorcraft turbulence. Turbulence filters merely shape the spectral form so that the required dispersions are delivered, while imposing a second-order high-frequency asymptote (for the Dryden spectral form of ref. 1). For a blade element rotor system, the implementation of the military specification filters produces an intractable modeling problem, because the filter's poles are cyclostationary. This is caused by the pole's direct proportionality with aerodynamic velocity. The problem is exemplified in the baseline model, which is used for comparison purposes. The DOBEST model, however, extracts the average poles for filter representations at each element location, and by use of a novel distribution algorithm, creates a very accurate field of filter inputs. For the rotor system, these inputs rotate with the blades and display the proper correlation at all aerodynamic centers in the rotorcraft model. The utilized filter coefficients adequately represent spectral variations owing to vehicle velocity and altitude variations, and do not distort the Gaussian characteristics of the input turbulent field.

THE GEOMETRY

Sikorsky's Black Hawk (ref. 2) model (GENHEL) is used as an example of a sophisticated rotorcraft model with aerodynamic representations at distributed locations, including elemental stations along each blade. Looking down on the rotorcraft, a circle of

diameter L is defined that includes the entire main rotor area and the tail rotor.

The techniques derived here may be extended to a volume of space about the vehicle, but this is not required. *“Because of the small vertical dimension of the airplane relative to the length and span, it is reasonable to ignore variations of the turbulence over the vertical dimension of the airplane”* (ref.1). The main rotor used here for illustration purposes is based on blade-element theory, and the tail rotor model is based on Bailey theory.

A coordinate system is created with respect to the rotorcraft x-y plane, which is different from the previously used coordinate system in the SORBET model of reference 3. In contrast to SORBET, the DOBEST model's coordinate system is independent of the wind axis. It does not use temporal buffers for velocity histories, because Taylor's hypothesis states that time variations in stochastic turbulence are statistically equivalent to distance variations in traversing a field of turbulence (ref. 1). The SORBET model, however, accommodates discrete gusts. Discrete gusts must be otherwise handled in the DOBEST model, and their application to the vehicle's aerodynamics does not involve the turbulence filters.

For certain kinds of experiments, there is interest in simulating rotorcraft responses corresponding to gusts over ship or terrain features; this is accomplished using an intermediate data-preparation step involving computational fluid dynamics (CFD). These simulations are intended to correlate the gust and turbulent field to the terrain as perceived by the pilot. The DOBEST model, however, only produces stochastic turbulence velocities. Energy-related parameters such as turbulence variances and dissipation rate (from a CFD analysis) would be required in order for DOBEST to augment a terrain-correlated application.

It is suggested that a model for responses to discrete gusts, as required in a terrain-correlated program, may use a nonrotating four-point application concept similar to that discussed here. For gust models, this requires a relatively small computational workload in the transmittal of the data necessary to compute accurate aircraft gust responses. For example, wind vectors at four points about the vehicle, in addition to turbulence intensities applicable for the entire rotorcraft (usually given by the dispersions σ_i), are sufficient to compute aircraft gust and turbulence responses for a distributed model. This statement assumes that the standard military specification atmospheric model is used for the turbulence scale lengths. In terrain-correlated

applications the turbulence wave number $\Omega_\theta = 1/L$ may alternatively be used. This quantity is related to the turbulence dissipation rate in “ $k - \varepsilon$ ” models, as discussed in reference 4. In this case the filter pole becomes $p = \Omega_\theta V$, where the components of Ω_θ are also applicable for the entire rotorcraft.

The four-point concept may benefit gust models such as that of reference 4, where the data-acquisition points should be distributed symmetrically about the rotorcraft at a radius equal to the square root of two times the outboard element radius r_s (in order to define a box around a rotor system that includes all element radii plus the tail rotor). By orienting the acquisition points along the vehicle horizontal axes, the position of the tail rotor is interior to the delineated area. The implied interpolation scheme, that is using simple geometrical relationships to the aerodynamic centers of a distributed model, is superior to the transmittal of atmospheric gradient data, because the aircraft’s geometry is then considered, and linearity between data points is not assumed. “*Also, it should be mentioned here that the aerodynamic effects of gust gradients are not quite the same as the effects of the airplane angular velocities*” (ref. 1). This is an important consideration in evaluating the performance of different vehicles in similar gust and turbulence environments.

For simplification in this derivation, the tail rotor is assumed to be coincident with the empennage and horizontal tail; also the main rotor hub is assumed to be coincident with the vehicle center-of-mass. These assumptions do not appear to be significant for the distribution of stochastic turbulence in the Black Hawk model. The techniques may be extended for models with different geometry, such as a rotorcraft with two main rotors, and with minimal computational workload, additional aerodynamic centers may be included by use of the distribution algorithm.

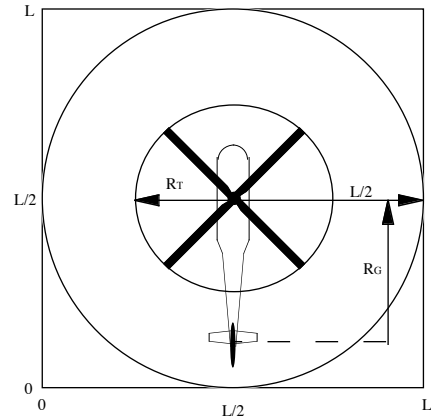


Figure 1. Introductory geometry.

In figure 1 a circle of diameter L is defined, where L is the symmetric characteristic scale length of turbulence in the vehicle x-y plane, which is a function of altitude. The rotor hub is located at the center of the circle, and the rotor radius R_T is a fraction of the radius $L/2$. The location of the tail rotor is also within the circle, because its distance from the rotor hub is less than $L/2$ for minimum L . From a military specification (ref. 5), the minimum value of L in the x-y plane is 75.64 ft. The distance from the main rotor hub to the tail rotor of the Black Hawk model is $R_G = 32$ ft .

The main rotor radius is $R_T = 26.83$ ft, which includes the hinge offset $e = 1.25$ ft and the spar length $e' = 2.25$ ft. Using the equal annuli algorithm of reference 2, the radius from the main rotor hub to a blade station, r_m , may be computed from

$$r_m = \sqrt{(e + e')^2 + \frac{2m-1}{2M} [R_T^2 - (e + e')^2]} - e$$

where the blades are modeled using $1 \leq m \leq M$ segments; nominally $M = 5$.

For five radial stations the equal annuli algorithm produces the radial positions (ft) and rotational velocities (ft/sec) shown in table 1.

Table 1. Element positions and rotational velocities.

m	r_m	$\Omega_T r_m$
1	7.86	212.25
2	13.73	370.83
3	17.88	482.83
4	21.28	574.54
5	24.23	654.14

The average element velocities used in the DOBEST model are never less than these rotational velocity components. A variable rotor rpm is not excluded in this model.

For most flight regimes the scale length L is large compared to the rotor diameter. In this case turbulence throughout the rotorcraft is highly correlated. However, at sea level L approaches the rotor diameter, in a proportion similar to that illustrated in figure 1. As is discussed, correlation then becomes a very important phenomenon.

THE DISTRIBUTION ALGORITHM

Four uncorrelated, unity-variance, zero-mean, Gaussian random variables ($\varepsilon_1, \varepsilon_2, \varepsilon_3, \varepsilon_4$) per translational axis are assumed available in the following derivation.

Independent noise sources are not necessarily required to create these variables in discrete simulation; sequential values from a single source with a long period may also be used. For all three axes, these variables may be represented by $(\varepsilon_1, \varepsilon_2, \varepsilon_3, \varepsilon_4)_k$, where $k = 1, 2, 3$ represents the vehicle's x-y-z axes.

Rotations are used to distribute these variables over both the rotor system and the vehicle geometry. A rotation matrix in the x-y plane is developed by weighting the independent variables as functions of their angles of rotation:

$$\mu_i = \sum_{j=1}^4 \left\{ a + b \cos \left[\psi_i + (j-1) \frac{\pi}{2} \right] \right\} \varepsilon_j$$

Using the expected value operator E , the Gaussian characteristics of the original noise sources (except independence) are preserved when

$$E\{\mu_i^2\} = 4a^2 + 2b^2 = 1$$

$$E\{\mu_i \mu_{i+2}\} = 4a^2 - 2b^2 = 0$$

These relationships yield $a = 1/\sqrt{8}$ and $b = 1/2$.

The rotations are functions of the azimuth angles of the individual blades, but may be written as a function of the azimuth angle of just one blade, ψ_1 . Where $S = \sin \psi_1$ and $C = \cos \psi_1$, the rotation matrix is

$$\begin{bmatrix} \mu_1 \\ \mu_2 \\ \mu_3 \\ \mu_4 \\ \mu_5 \\ \mu_6 \end{bmatrix} = \frac{1}{\sqrt{8}} \begin{bmatrix} 1 + \sqrt{2}C & 1 + \sqrt{2}S & 1 - \sqrt{2}C & 1 - \sqrt{2}S \\ 1 - \sqrt{2}S & 1 + \sqrt{2}C & 1 + \sqrt{2}S & 1 - \sqrt{2}C \\ 1 - \sqrt{2}C & 1 - \sqrt{2}S & 1 + \sqrt{2}C & 1 + \sqrt{2}S \\ 1 + \sqrt{2}S & 1 - \sqrt{2}C & 1 - \sqrt{2}S & 1 + \sqrt{2}C \\ 1 + \sqrt{2} & 1 & 1 - \sqrt{2} & 1 \\ 1 - \sqrt{2} & 1 & 1 + \sqrt{2} & 1 \end{bmatrix} \begin{bmatrix} \varepsilon_1 \\ \varepsilon_2 \\ \varepsilon_3 \\ \varepsilon_4 \end{bmatrix}$$

Note that six correlated variables have been created from the original four uncorrelated variables (per axis). These six variables remain unity-variance, zero-mean, Gaussian random variables.

As illustrated in figure 2, the first four rotated variables in the above set are associated with individual blades, whereas the latter two rotated variables are associated with the vehicle's longitudinal body axis. The rotated variables are in a plane coincident with the vehicle's longitudinal and lateral axes, on a circle of diameter L . The application points of the first four variables are extensions of the four blades, at a radius $L/2$ from the rotor hub; L has a minimum value of 75.64 ft.

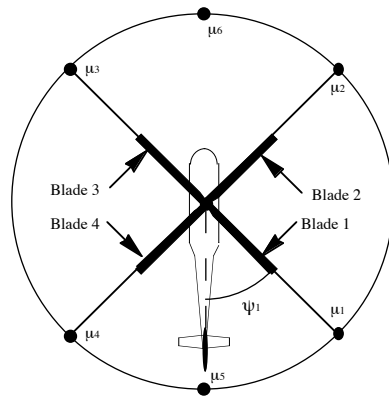


Figure 2. Random variable locations.

The latter two longitudinal random variables do not rotate with the rotor system, and are used to create random variables along the longitudinal body axis. If the lateral dimension of the aircraft also has significant aerodynamic centers, two lateral variables may easily be defined. For example, variables μ_7 and μ_8 may be created for this purpose. They would be similar to μ_5 and μ_6 , but rotated 90 degrees. All aerodynamic centers represented in a distributed rotorcraft model are then accommodated by use of these variables. The

body-fixed variables display the proper statistical relationships with respect to the rotor system variables.

For each of the rotated random variables, either along the longitudinal axis or distributed on the rotating blades, the variance is unity,

$$E\{\mu_i^2\} = 1$$

For random variables with the above characteristics the correlation coefficient between individual components is also the covariance. For opposing-blade and body-axis random variables the covariances are all zero,

$$E\{\mu_1\mu_3\} = E\{\mu_2\mu_4\} = E\{\mu_5\mu_6\} = 0$$

However, considering the rotor system, adjacent blades are correlated, and their covariances are given by

$$E\{\mu_1\mu_2\} = E\{\mu_1\mu_4\} = E\{\mu_2\mu_3\} = E\{\mu_3\mu_4\} = \frac{1}{2}$$

From the above relationships, the random variable at the hub may be expressed by,

$$\mu_0 = \frac{1}{\sqrt{8}} \sum_{i=1}^4 \mu_i = \frac{1}{\sqrt{2}} (\mu_5 + \mu_6) = \frac{1}{2} \sum_{i=1}^4 \varepsilon_i$$

The covariance from the hub to any of the six random variables is

$$E\{\mu_0\mu_i\} = \sqrt{\frac{1}{2}}$$

CORRELATION

The distance L is the characteristic length of turbulence in the vehicle's x-y plane, and this length defines the distance at which the correlation between points vanishes. Hence, for two points separated by a distance $2r_m$, the correlation between zero-mean, unity-variance variables at these points may be defined by a function that is unity when they are coincident, and zero when their separation is equal to the characteristic scale length. Defining a normalized distance between two identical-radius segments on opposing blades,

$$d_m = \frac{2r_m}{L}$$

an exponential correlation coefficient is defined that meets these requirements:

$$\rho_m = (1 - d_m)e^{-d_m}$$

A compatible linear form is also examined.

These definitions permit the use of a novel interpolation algorithm for the creation of random variables at all blade-element locations, and the variables have the same unity variances and zero means. Turbulence filters are then applied at each element location, because their inputs are unique. However, considerable simplification occurs in the DOBEST model because the utilized velocity of all four blades is identical at any given radial station. The DOBEST model makes use of the fact that Gaussian variables passing through linear filters remain Gaussian. This is not true if cyclostationary filters are used, as is the case in the baseline model.

The Black Hawk has $N = 4$ blades, and each element on each blade contributes forces (and hence moments) to the total rotorcraft model. In the DOBEST model the filter poles are a function of only the radial index ($m = 1, 2, 3, 4, 5$), and not the blade index ($n = 1, 2, 3, 4$).

Because the velocities V_m have been defined (see appendix A) as independent of ψ_n , only five sets of filter coefficients are required for each of the three rotor system axes. For the blade elements, 20 separate inputs are created from the interpolation scheme (from four random variables) per axis. This algorithm is a two-dimensional extension of earlier work described in references 3 and 6.

Figure 3 identifies the locations at which the rotated variables (μ_i) are used, in order to create variables (η_i) applicable at the various radial and body-axis stations. The rotor system is discussed first, where the variables ($\eta_{1,m}, \eta_{2,m}, \eta_{3,m}, \eta_{4,m}$) are created in the rotating frame for each of the three aircraft dimensions.

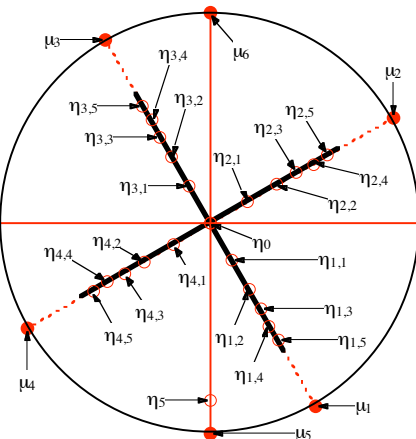


Figure 3. Distributed random variables.

From the four blade variables per dimension, the hub variable $\eta_0 = \mu_0$ is created per dimension, which is generalized here to be the center-of-mass variable. For locations along the x-body axis the additional variables μ_5 and μ_6 are required in order to interpolate the covariances. In this simplified model these two variables are used to create a correlated random variable η_5 (per dimension) at the location of the tail rotor.

THE ROTOR SYSTEM

Since the rotation matrix is a cyclic function of time, the random variables μ_i contain periodic behavior in sampling the original noise sources ε_i . In this section the individual blade-element random variables of figure 3 ($\eta_{n,m}$) are developed; they also contain the periodic behavior. This distribution thus yields an accurate description of the random noise sources at each rotating blade-element location.

Where the first index identifies a particular blade, for any element the random variable at r_m is $\eta_{n,m}$,

$$\begin{aligned}\eta_{1,m} &= A_m \mu_1 + B_m \mu_3 \\ \eta_{2,m} &= A_m \mu_2 + B_m \mu_4 \\ \eta_{3,m} &= A_m \mu_3 + B_m \mu_1 \\ \eta_{4,m} &= A_m \mu_4 + B_m \mu_2\end{aligned}$$

where the coefficients are

$$\begin{aligned}A_m &= \frac{1}{2} \left(\sqrt{1 + \rho_m} + \sqrt{1 - \rho_m} \right) \\ B_m &= \frac{1}{2} \left(\sqrt{1 + \rho_m} - \sqrt{1 - \rho_m} \right)\end{aligned}$$

In computing the covariance between any point r_{n_1,m_1} and another point r_{n_2,m_2} , general relationships exist, depending only on the blade indices. For the same blade, adjacent blades and opposing blades, these covariances are, respectively,

$$E\{\eta_{n_1,m_1} \eta_{n_2,m_2}\} = \begin{cases} A_{m_1} A_{m_2} + B_{m_1} B_{m_2} & |n_1 - n_2| = 0 \\ \frac{1}{2} (A_{m_1} + B_{m_1}) (A_{m_2} + B_{m_2}) & |n_1 - n_2| = 1, 3 \\ A_{m_1} B_{m_2} + A_{m_2} B_{m_1} & |n_1 - n_2| = 2 \end{cases}$$

For any segment on any blade the variance is

$$E\{\eta_{n,m}^2\} = A_m^2 + B_m^2 = 1$$

When blades are adjacent, as in the following example, the covariance between equal-radius elements is given by

$$\rho_{14,m} = E\{r_{1,m} r_{4,m}\} = \frac{1}{2} (A_m + B_m)^2 = \frac{1}{2} (1 + \rho_m)$$

The same equation computes $\rho_{12,m}$, $\rho_{23,m}$ and $\rho_{34,m}$, where blade indices such as "12" are interchangeable. When the blades oppose each other, the covariances are

$$\begin{aligned}\rho_{13,m} &= E\{r_{1,m} r_{3,m}\} = 2A_m B_m = \rho_m \\ \rho_{24,m} &= E\{r_{2,m} r_{4,m}\} = 2A_m B_m = \rho_m\end{aligned}$$

These covariances vanish if a radial station r_m could be as large as $L/2$, where ρ_m vanishes, and they approach unity as the radial stations approach the rotor hub, where ρ_m approaches unity (d_m vanishes).

The covariances are illustrated in figure 4. Also included is the covariance between the hub and radii from the hub. For low-altitude flight, a blade's elemental stations are given as solid circles and the tail is given as an open circle. As altitude increases, the value for L increases such that d_m decreases. These points thus migrate toward the ordinate with increasing altitude, and the elements receive more correlated inputs.

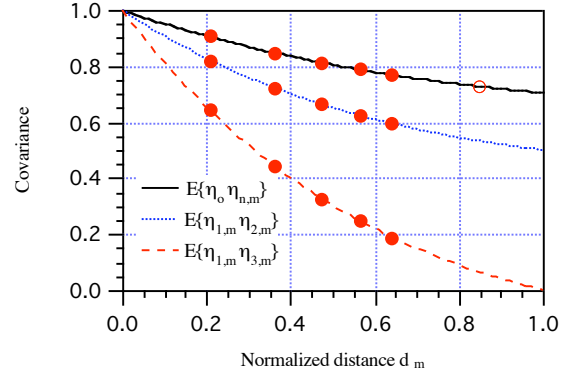


Figure 4. Covariances.

At the outboard blade-element station for the Black Hawk's rotor model, the largest possible value is $d_s = 0.641$, at sea level. At an altitude of 1,000 ft the value decreases to $d_s = 0.048$. As indicated in figure 4, the rotor inputs become more correlated for high altitudes, because the points migrate to the left (L gets larger so d_m gets smaller). However, as shown in figure 4, correlation is important for low-altitude flight. Element disturbances become less correlated, and this causes an increase in the vehicle's rotational activity, as will be shown.

If a linear formulation for the covariance was used,

$$\rho_m = 1 - d_m$$

the covariances would become as shown in figure 5.

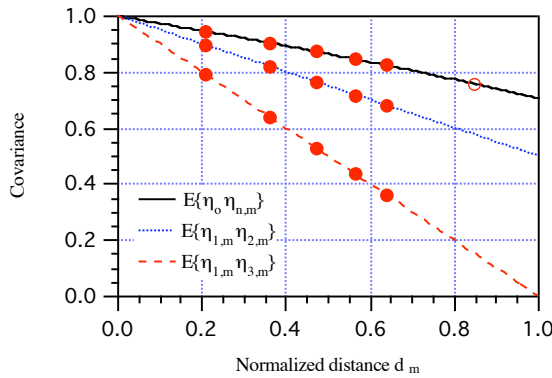


Figure 5. Alternative covariances.

The linear formulation produces more correlation between the blade elements, and this produces less rotational activity at all altitudes. The linear form is that discussed in reference 1, although those authors probably never envisioned helicopter applications. It is useful to keep in mind the “tweaking” that is usually required. From reference 1: “The turbulence model ... has been developed by rather arbitrarily choosing reasonable values of the scales and then determining values for the intensity so that the mathematical spectral form ... fits the measured spectral data ...”.

THE CENTER OF MASS

Where the hub position is given as $r_0 = 0$, the coefficients become

$$A_0 = B_0 = \frac{1}{\sqrt{2}}$$

and the three previously shown covariance relationships collapse to a single relationship. The covariance between the hub and any segment of any blade is

$$\rho_{0,m} = E\{\eta_0 \eta_{m,n}\} = \frac{1}{\sqrt{2}}(A_m + B_m) = \sqrt{\frac{1 + \rho_m}{2}}$$

The random variable and variance at the hub are

$$\eta_0 = \mu_0 = \frac{1}{\sqrt{2}}(\mu_5 + \mu_6)$$

$$E\{\eta_0^2\} = 1$$

Assuming this point to be coincident with the vehicle center of mass, η_0 becomes the center-of-mass random variable, properly correlated with the blade's random

variables. However, neither the hub nor the tail rotates with the blades, so their turbulence filters must use an alternative velocity specification (the true airspeed V_{RW}) to that used by the rotor system's individual elements.

THE TAIL

In order to create turbulence at the tail, interpolation is used between μ_5 and μ_6 . These independent variables are also located at a distance $L/2$ from the hub, but are not rotating with the blades. As above, a correlation distance and coefficient are defined:

$$d_T = \frac{2r_G}{L}$$

$$\rho_T = (1 - d_T)e^{-d_T}$$

As in the formulation for the individual blade elements, the coefficients become,

$$A_T = \frac{1}{2}(\sqrt{1 + \rho_T} + \sqrt{1 - \rho_T})$$

$$B_T = \frac{1}{2}(\sqrt{1 + \rho_T} - \sqrt{1 - \rho_T})$$

The tail's random variable and covariance between the hub and tail are given by

$$\eta_5 = A_T \mu_5 + B_T \mu_6$$

$$\rho_{0T} = E\{\eta_0 \eta_5\} = \sqrt{\frac{1 + \rho_T}{2}}$$

For the Black Hawk model at sea level $d_T = 0.8461$, $\rho_T = 0.066$ and $\rho_{0T} = 0.73$. At the outboard segment for adjacent blades the correlation drops to 0.595, and for opposing blades it drops to 0.189.

All of the cross-correlations are shown in figure 6.

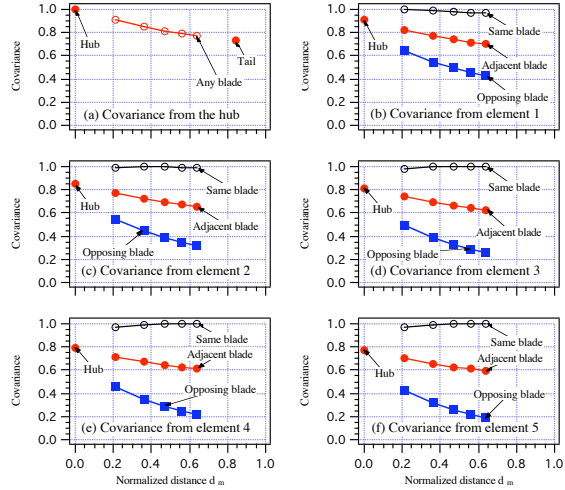


Figure 6. Cross correlations.

All of the indicated points migrate toward the ordinates of these graphs with increasing altitude.

Correlations between the individual elements and the tail are not shown in figure 6 because they are periodic functions of azimuth angle:

$$\begin{aligned}
 E\{\eta_5 \eta_{1,m}\} &= \frac{1}{2} \left[\sqrt{(1 + \rho_T)(1 + \rho_m)} + \sqrt{(1 - \rho_T)(1 - \rho_m)} \cos \psi_1 \right] \\
 E\{\eta_5 \eta_{2,m}\} &= \frac{1}{2} \left[\sqrt{(1 + \rho_T)(1 + \rho_m)} - \sqrt{(1 - \rho_T)(1 - \rho_m)} \sin \psi_1 \right] \\
 E\{\eta_5 \eta_{3,m}\} &= \frac{1}{2} \left[\sqrt{(1 + \rho_T)(1 + \rho_m)} - \sqrt{(1 - \rho_T)(1 - \rho_m)} \cos \psi_1 \right] \\
 E\{\eta_5 \eta_{4,m}\} &= \frac{1}{2} \left[\sqrt{(1 + \rho_T)(1 + \rho_m)} + \sqrt{(1 - \rho_T)(1 - \rho_m)} \sin \psi_1 \right]
 \end{aligned}$$

TURBULENCE FILTERS

The filter inputs developed in the preceding sections are properly correlated. The blade-element inputs even contain rotary effects in sampling random noise. In fact, the problem of creating rotorcraft turbulence would be completely solved by the above operations if a constant relationship existed between the distributed noise and the resultant turbulence velocities. Alas, Taylor *et al.* determined that transfer functions are required, and those functions consist of filters that have coefficients that are functions of altitude and airspeed. For a rotor system, where element velocities are nonlinear, the airspeed functionality presents an unusual modeling challenge.

In the previous sections a field of random variables has been created that displays the proper correlation between the aerodynamic centers of the rotorcraft. For example, as a blade passes the aft azimuth position, its

outboard element receives inputs that are almost identical to those received by the tail rotor.

By passing these inputs through *linear* filters the power spectral densities are shaped, while the correlation is retained. The shaping function is based on a pass band, which is determined by the filter pole. In the next section the rotor systems filters are determined to be second order. However, first-order systems seem to be gaining some popularity in terrain- and ship-correlated applications. Computer science techniques are used to produce low-pass filters that avoid significant aliasing. This is alluded to in the literature: “*To ensure stability of the real-time turbulence filters, the model software includes safeguards that limit the frequencies of the*

filters to a magnitude not greater than one-quarter of the simulation sampling frequency.” This is equivalent to sampling the random variables every four computer cycles, and seems to be an effective technique for producing sharply attenuated low-pass responses.

From references 1, 5 and 7, Table 2 is presented to show the parameters to be used in turbulence filters according to the Dryden spectral form in military specifications (the references are shown in the table).

Table 2. Dryden spatial PSD specifications.

	<i>Ref. 1, 1969</i>	<i>Ref. 5, 1980</i>	<i>Ref. 7, 1990</i>
L_u	$\begin{cases} 145h^{1/3} & h < 1750 \\ 1750 & h \geq 1750 \end{cases}$	$\begin{cases} 75.64 & h \leq 10 \\ hf_h^{-1/2} & 10 < h \leq 1000 \\ h & 1000 < h \leq 1750 \\ 1750 & h \geq 1750 \end{cases}$	$\begin{cases} 75.64 & h \leq 10 \\ hf_h^{-1/2} & 10 < h \leq 1000 \\ h & 1000 < h \leq 1750 \\ 1750 & h \geq 1750 \end{cases}$
L_v	$\begin{cases} 145h^{1/3} & h < 1750 \\ 1750 & h \geq 1750 \end{cases}$	$\begin{cases} 75.64 & h \leq 10 \\ hf_h^{-1/2} & 10 < h \leq 1000 \\ h & 1000 < h \leq 1750 \\ 1750 & h \geq 1750 \end{cases}$	$\begin{cases} 3782 & h \leq 10 \\ \frac{1}{2}hf_h^{-1/2} & 10 < h \leq 1000 \\ \frac{h}{2} & 1000 < h \leq 1750 \\ 875 & h \geq 1750 \end{cases}$
L_w	$\begin{cases} h & h < 1750 \\ 1750 & h \geq 1750 \end{cases}$	$\begin{cases} 10 & h \leq 10 \\ h & 10 < h \leq 1750 \\ 1750 & h > 1750 \end{cases}$	$\begin{cases} 5 & h \leq 10 \\ \frac{h}{2} & 10 < h \leq 1750 \\ 875 & h > 1750 \end{cases}$
σ_u, σ_v	$\sigma_w \sqrt{\frac{L_u}{L_w}}$	$\begin{cases} \sigma_w f_h^{-0.4} & h < 1000 \\ \sigma_w & h \geq 1000 \end{cases}$	$\begin{cases} \sigma_w f_h^{-0.4} & h < 1000 \\ \sigma_w & h \geq 1000 \end{cases}$
$\Phi_u(\Omega)$	$\frac{2L_u\sigma_u^2}{\pi[1+(L_u\Omega)^2]}$	$\frac{2L_u\sigma_u^2}{\pi[1+(L_u\Omega)^2]}$	$\frac{2L_u\sigma_u^2}{\pi[1+(L_u\Omega)^2]}$
$\Phi_v(\Omega)$	$\frac{L_v\sigma_v^2[1+3(L_v\Omega)^2]}{\pi[1+(L_v\Omega)^2]^2}$	$\frac{L_v\sigma_v^2[1+3(L_v\Omega)^2]}{\pi[1+(L_v\Omega)^2]^2}$	$\frac{2L_v\sigma_v^2[1+3(2L_v\Omega)^2]}{\pi[1+(2L_v\Omega)^2]^2}$
$\Phi_w(\Omega)$	$\frac{L_w\sigma_w^2[1+3(L_w\Omega)^2]}{\pi[1+(L_w\Omega)^2]^2}$	$\frac{L_w\sigma_w^2[1+3(L_w\Omega)^2]}{\pi[1+(L_w\Omega)^2]^2}$	$\frac{2L_w\sigma_w^2[1+3(2L_w\Omega)^2]}{\pi[1+(2L_w\Omega)^2]^2}$

The function of altitude f_h appearing in this table is given by

$$f_h = 0.177 + 0.000823h$$

Upon inspection of Table 2, the 1990 formulation is equivalent to the 1980 formulation. The halved scale lengths (L_v, L_w) in the 1990 model have been accommodated by a redefinition of the spectral characteristics. This confusing notation shift is ignored here, and the 1980 formulation is used. The scale lengths L_u and L_v in the x-y plane are then identical. Furthermore, since the DOBEST model makes no distinction in the direction of travel, Φ_u collapses to Φ_v . The required parameters for the turbulence filters then become,

$$L = L_u = L_v = \begin{cases} 75.64 & h \leq 10 \\ hf_h^{-1/2} & 10 < h \leq 1000 \\ h & 1000 < h \leq 1750 \\ 1750 & h \geq 1750 \end{cases}$$

$$L_w = \begin{cases} 10 & h \leq 10 \\ h & 10 < h \leq 1750 \\ 1750 & h > 1750 \end{cases}$$

$$\sigma = \sigma_u = \sigma_v = \begin{cases} \sigma_w f_h^{-0.4} & h \leq 1000 \\ \sigma_w & h > 1000 \end{cases}$$

For the rotor system the spatial spectra all become

$$\Phi_{[U,V,W]}(\Omega) = \frac{L_i \sigma_i^2 [1 + 3(L_i \Omega)^2]}{\pi [1 + (L_i \Omega)^2]^2}$$

Hence, all of the Laplace filters have the same form. They are given by the critically damped systems,

$$u_m(s) = v_m(s) = \frac{\sigma \sqrt{3V_m / \pi L} (s + V_m / \sqrt{3}L)}{(s + V_m / L)^2}$$

$$w_m(s) = \frac{\sigma_w \sqrt{3V_m / \pi L_w} (s + V_m / \sqrt{3}L_w)}{(s + V_m / L_w)^2}$$

Using the Dryden form these filters are developed by decomposing $\Phi(\Omega)$ into a function $\phi(j\omega)$ times its conjugate, and the Laplace forms are extracted. This process is more complicated for the von Karman spectral form. “*The Dryden form has been chosen because it is simple to mechanize, as opposed to the von Karman form that must be approximated to become realizable*” (ref. 7). The von Karman form is also used at Ames Research Center.

In the next section the minimum value for L_w is shown to be larger than the value of 10 ft given in table 2 using realistic cycle times, owing to sample data phenomena.

BANDWIDTH CONSIDERATIONS

The bandwidth of a system is defined as that range of frequencies over which the system responds “satisfactorily.” For real-time, piloted flight simulations the bandwidth of the response to turbulence must not be too large. Considering NASA’s Vertical Motion Simulator (VMS) located at Ames Research Center, faithful responses cannot occur beyond a few Hertz. Motion drive motors are usually isolated from higher frequency inputs by protective filters. Nonetheless, residual high frequencies can be unrealistic. Using the VMS and a conventional turbulence formulation, one pilot’s comment concerning hover performance was “*It was like a washboard*” (ref. 3). Often-desired high-frequency inputs, such as the N/rev phenomenon (see ref. 8) of about 17 Hz, are sometimes relegated to seat shakers. The magnitude of this signal may be isolated, and filtered (ref. 9) from the rotor contributions to vehicle dynamics.

The basic problem with a high bandwidth, however, has to do with the discrete modeling of transfer functions that were developed using conventional aircraft parameters. For this discussion we need a couple of

quantities. Defining the “pole” and its discrete equivalent,

$$p = \frac{V}{L}$$

$$\alpha = p\Delta t$$

the Laplace transfer function representing unity-dispersion turbulence may be written

$$f(s) = \frac{A_\omega (s + p/\sqrt{3})}{(s + p)^2}$$

Its power spectral density is given by

$$|f(j\omega)|^2 = \frac{A_\omega^2 (\omega^2 + p^2 \beta)}{(\omega^2 + p^2)^2}$$

By integrating the spectrum, the total power is determined, and it must be unity:

$$P_\omega = 1 = \int_0^\infty |f(j\omega)|^2 d\omega = \frac{A_\omega^2 \pi}{3p}$$

From this expression the continuum gain is produced,

$$A_\omega = \sqrt{\frac{3p}{\pi}}$$

For a discrete system, the zero-order data-hold formulation is used for both stability and accuracy,

$$F(z) = Z \left\{ \left(\frac{1 - e^{-s\Delta t}}{s} \right) f(s) \right\}$$

This produces the z-transform

$$F(z) = \frac{A_\omega (Bz + C)}{\sqrt{3}p(z - e^{-\alpha})^2}$$

In this equation the coefficients are

$$B = 1 - e^{-\alpha} + (\sqrt{3} - 1)\alpha e^{-\alpha}$$

$$C = e^{-2\alpha} - e^{-\alpha} - (\sqrt{3} - 1)\alpha e^{-\alpha}$$

The discrete power spectral density is given by

$$|F(e^{j\omega\Delta t})|^2 = \frac{A_\omega^2 (B^2 + C^2 + 2BC \cos \omega \Delta t)}{3p^2 (1 + e^{-2\alpha} - 2e^{-\alpha} \cos \omega \Delta t)^2}$$

By integrating this spectrum to the Nyquist frequency the total power in discrete simulation is computed:

$$P_z = \frac{1}{\Delta t} \int_0^{\pi} \left| F(e^{j\omega\Delta t}) \right|^2 d(\omega\Delta t)$$

This produces

$$P_z = \frac{\pi A_\omega^2 (1-e^{-\alpha})^2 \left\{ (\sqrt{3}-1)^2 \alpha^2 e^{-2\alpha} + [(\sqrt{3}-1)\alpha e^{-\alpha} + 1 - e^{-2\alpha}]^2 \right\}}{3p\alpha(1-e^{-2\alpha})^3}$$

Substituting the continuum gain, the total power obtained in simulation is seen to be a function of only the equivalent discrete pole α , and is in general, not unity:

$$P_z = \frac{(1-e^{-\alpha})^2 \left\{ (\sqrt{3}-1)^2 \alpha^2 e^{-2\alpha} + [(\sqrt{3}-1)\alpha e^{-\alpha} + 1 - e^{-2\alpha}]^2 \right\}}{\alpha(1-e^{-2\alpha})^3}$$

The degradation in total discrete power is shown in figure 7.

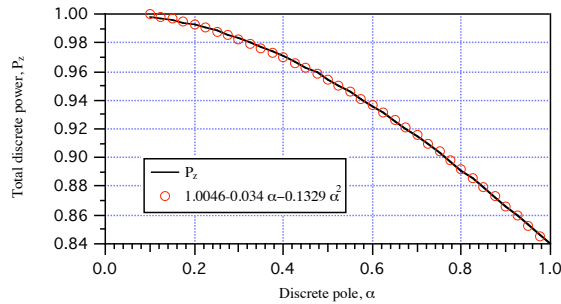


Figure 7. Degradation in total discrete power.

Also shown in figure 7 is a second-order curve fit to P_z , which is quite accurate in the indicated range.

Of course, the discrete gain could be normalized, and this would produce unity total power in discrete simulation. However, this invariably amplifies the spectrum over the discrete bandwidth. This is shown in figure 8, where the discrete curves extend only to the Nyquist frequency of 50 Hz.

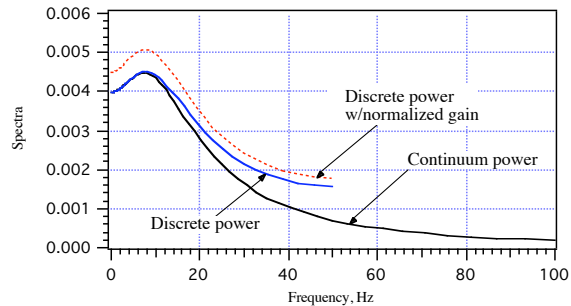


Figure 8. Spectral comparisons, $\alpha = 0.8$.

The value $\alpha = 0.8$ was used to create figure 8. The total power is the integral under these curves, and since the continuum curve extends to infinity, its area (of unity) is greater than that of the curve tagged "Discrete Power," which is $P_z = 0.8914$ in figure 8. The curve tagged "Discrete Power w/Normalized Gain" has the desired unity total power, but the accompanying distortion is not acceptable.

As is indicated by figure 8, the continuum gain A_ω must be retained in order to preserve the frequency response over a significant portion of the discrete bandwidth. Hence, α must be limited, and as is shown below, this implies that, for the rotor system transfer functions, L_ω must have a minimum value that is greater than the value of 10 ft given in table 2. This conclusion is not the result of atmospheric physics; it is simply the result of sampled data theory. If the sample period could be significantly reduced below the value of 0.01 sec, then limiting L_ω for the rotor's filters would not be required.

Similar problems have arisen in the discrete simulation of rotor systems throughout the years. For example, reference 8 describes the undesirable aliasing phenomenon associated with cycle times that are too large to accommodate the high frequencies that are generated in a rotor system.

Essentially, problems arise in the discrete simulation of a transfer function when the discrete spectrum magnitude remains significant at frequencies that are an appreciable fraction of the Nyquist frequency (usually as observed on a log-frequency plot), such that manifest aliasing occurs.

As may be seen in figure 9, a lower limit on the discrete pole of about $\alpha \leq 0.25$ will preserve about 98.83% of the total power. When this change is made, figure 8 is transformed into figure 9, where $\alpha = 0.25$.

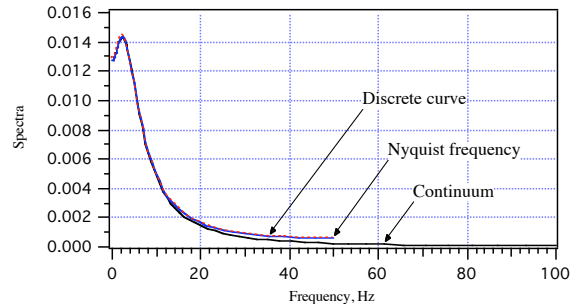


Figure 9. Spectral comparisons, $\alpha = 0.25$.

The loss of total power by allowing α to be somewhat larger than 0.25 does not seem to severely influence

time histories, but it does alter the covariances in the rotor system. That is, observed cross correlations using spectral techniques depart from their theoretical values because of the disproportionate loss in power at the outboard segment locations. Thus, from a purely mathematical point of view, the artifact of placing a lower limit on L_w in the rotor computations of the DOBEST model is justified. This produces an upper limit on the pole size

$$\alpha_{\max} = 0.25 = p_{\max} \Delta t \geq \frac{V_{n,m} \Delta t}{L_{\min}}$$

This limitation permits the realization of an accurate discrete solution that accomplishes the original goals of the filters:

1. Normalize the total power delivered so that meaningful dispersions may be applied
2. Produce a critically damped solution from the denominator polynomial of the filter
3. Produce a second-order roll off beyond the pass band in conformance with the Dryden atmospheric spectral relationships
4. Produce relatively flat responses for frequencies in the pass band
5. Retain the Gaussian characteristics of the input noise through the filters such that all of the covariance relationships given here apply to the filtered outputs

These goals are not met if the equivalent discrete pole takes liberties with sampled data theory. Hence, the discrete pole has an upper limit given by α_{\max} , atmospheric physics notwithstanding. It should be kept in mind that the above analysis is for a static system. The upper limit on the discrete pole does not eliminate the divergence inherent in the baseline model, which is caused by α periodically becoming too small (vanishing velocity).

As shown in appendix A for the baseline model, the maximum element velocity is available from any blade's outboard element:

$$V_{n,5} = \Omega_T r_5 + V_{RW}$$

Assuming $\Delta t = 0.01$ sec, this equation, combined with the above inequality for α_{\max} , produces a minimum value for the characteristic length:

$$L_{\min} \geq 26.2 + V_{RW}/25$$

This value only rises to 38.2 ft at a velocity of 300 ft/sec, so that it is invariably below the limit of 75.64 ft imposed in table 2 for L (L_u or L_v). Hence, the limit only applies to the vertical characteristic length used by the rotor system filters, L_w .

In the DOBEST model the maximum element velocity is always less than or equal to the maximum of the baseline model. Hence, the lower limit on L_w produces an even more reasonable range for α in the DOBEST model.

NOISE SOURCE CONSIDERATIONS

In the previous section a z-transform relationship was developed. Such relationships relate an input "x" to an output turbulence velocity "v". Operations were performed to produce the total power P_z , where these operations assumed that the input "x" had a unity total power integral. Otherwise "v" is biased by the input. This must be considered in order to create the correct gain for a difference equation driven by a noise source. For instance, the relationship may be written as

$$F(z) = \frac{A_\omega (Bz + C)}{\sqrt{3}p(z - e^{-\alpha})^2} = \frac{v(z)}{x(z)}$$

where $x(z)$ is computed from a noise source $\eta(z)$ with non-unity total power. In particular, a noise source called XNORM is used at Ames Research Center. It produces values with a Gaussian magnitude distribution in the range ± 3.45 when the dispersion is unity; this range includes 99.95% of the continuous probability integral. For the frequency distribution, the power spectral density is flat (white) over the discrete bandwidth, and is given by

$$\left| \Phi_\eta(\omega) \right|^2 = \begin{cases} 0 & \omega < 0 \\ \Delta t / \pi & 0 \leq \omega \leq \pi / \Delta t \\ 0 & \omega > \pi / \Delta t \end{cases}$$

The power is thus a constant over the Nyquist range, and in terms of noise values $\eta(z)$ created by XNORM they may be used in the above z-transform only if

$$\eta(z) = x(z) / \left| \Phi_\eta(\omega) \right| = \sqrt{\frac{\Delta t}{\pi}} x(z)$$

Hence, with respect to noise inputs with unity variance, the z-transform for velocity becomes

$$\frac{v(z)}{\eta(z)} = \left(\sqrt{\frac{\pi}{\Delta t}} \frac{A_\omega}{\sqrt{3}p} \right) \frac{(Bz + C)}{(z - e^{-\alpha})^2} = \sqrt{\frac{1}{p\Delta t}} \frac{(Bz + C)}{(z - e^{-\alpha})^2}$$

The difference equation for real-time simulation, including the dispersion, is then given by

$$v_{i+1} = 2e^{-\alpha} v_i - e^{-2\alpha} v_{i-1} + \sigma \sqrt{\frac{1}{\alpha}} (B\eta_i + C\eta_{i-1})$$

A procedure is given in appendix C for the discrete implementation of the DOBEST model in real-time simulation. The baseline model is essentially the same as this model, multiplied by a factor of 20 because the velocity of each element is computed independently. Although the workload of the baseline model does not necessarily preclude real-time simulation, its divergent responses and energy metrics do (see appendix B).

If first-order filters are used, as in reference 4, they are typically represented by

$$f(s) = \frac{\sigma \sqrt{2p/\pi}}{s+p}$$

Considering the spectrum of the noise source, this results in the z-transform relationship

$$\frac{v(z)}{\eta(z)} = \sigma \sqrt{\frac{2}{p\Delta t}} \left(\frac{1 - e^{-p\Delta t}}{z - e^{-p\Delta t}} \right)$$

However, if the noise source is sampled only every k^{th} cycle, the z-transform becomes

$$\frac{v(z)}{\eta(z)} = \sigma \sqrt{\frac{2}{kp\Delta t}} \left(\frac{1 - e^{-p\Delta t}}{z - e^{-p\Delta t}} \right)$$

PERFORMANCE

Turbulence velocities are developed in the DOBEST model as shown in appendix C. For example, considering the vertical axis of a blade, an element's turbulence velocity with respect to its input is given by a z-transform relationship that is only a function of the radial index:

$$\frac{w_{n,m}}{\eta_{n,m}} = F(z,m)$$

Through the aerodynamic relationships at each element station, a force is produced that is proportional to this velocity, which produces a torque depending on the moment arm. For rolling moments, the moment arms are the lateral distance from the hub, such that each element produces a torque proportional to

$$M_{n,m} \propto w_{n,m} r_m \sin\psi_1$$

Using the previous convention for $S = \sin\psi_1$ and $C = \cos\psi_1$, the vehicle's total roll torque is thus proportional to

$$M = \sum_{n=1}^4 \sum_{m=1}^5 M_{n,m} \propto \sum_{m=1}^5 r_m [S(w_{1,m} - w_{3,m}) + C(w_{2,m} - w_{4,m})]$$

The roll torque proportionality is a function of L_w (or altitude), an example of which is given in figure 10. Low, medium and high altitude cases are presented, where $\sigma_w = 1 \text{ ft/sec}$. The vertical velocities in figures 10a, 10c, and 10e are shown for just one blade, but all five segments are included. Although these segment velocity traces are overlaid, the magnitude decrease with altitude is clear.

The resultant roll torque magnitudes are shown in figures 10b, 10d, and 10f. Torque is shown to decrease in magnitude with altitude, and, because the filter inputs become more correlated with altitude, torque also changes its characteristics. The dominating frequency component is one-per-rev, and this is produced by the trigonometric functions in the above torque summation equation. The airspeed used to create these graphs was 200 ft/sec.

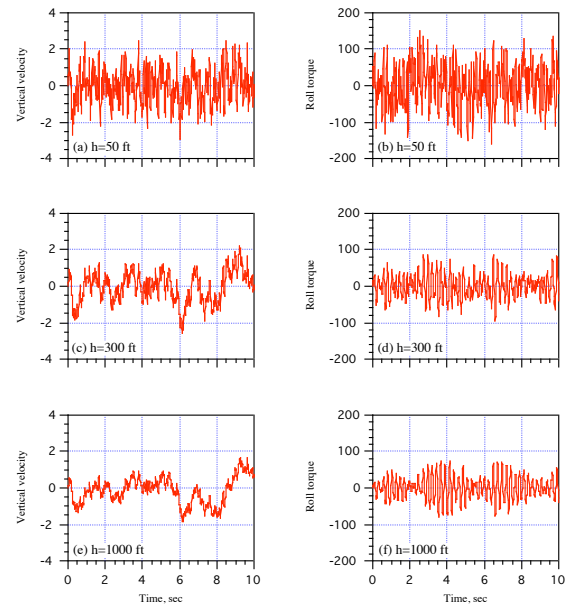


Figure 10. Vertical velocities and roll torque.

The input Gaussian noise histories were repeated for each of the flight conditions shown in figure 10. This means that the random variable inputs ε_i were identical for each case. Since L is a function of altitude, the interpolation coefficients are also functions of altitude. Hence, the correlations between the random variables

$\eta_{n,m}$ are also functions of altitude. The vertical turbulence filters use the characteristic length L_w , which is also a function of altitude. The observed response differences are therefore caused entirely by altitude variations.

The spectra from figure 10 (created by using a long time-history) are presented in figure 11. The vertical velocity spectra for each of the five segments (of one blade) are presented in figures 10a, 10c, and 10e. Roll torque spectra are presented in figures 11b, 11d, and 11f. When the altitude is low, as in figures 11a and 11b, the spectra are essentially flat out to about the rotor rpm. This occurs because the correlation between inputs is low. As altitude increases, the correlation between inputs gets larger, and the spectral magnitude gets smaller. As shown in figures 11d and 11f, the rpm then dominates the frequency response.

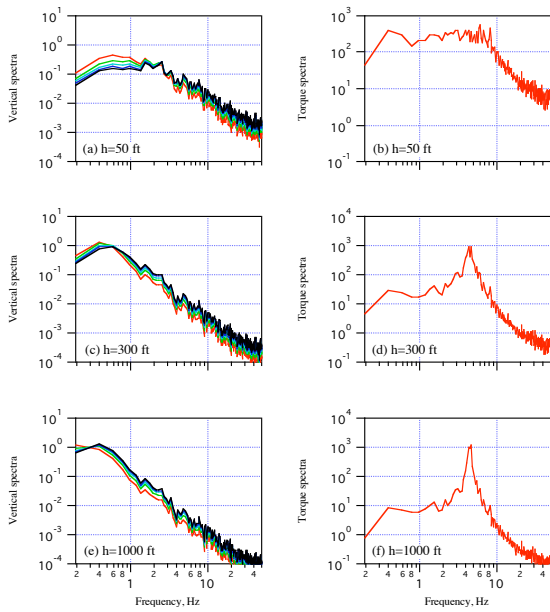


Figure 11. Vertical and roll spectra.

These isolated responses of rotor turbulence generated by DOBEST are relatively insensitive to the airspeed, which in these cases was 200 ft/sec. This insensitivity is discussed in appendix B. Similar torque histories occur for the pitch axis. The yaw axis is relatively insensitive to rotor turbulence for a fully articulated rotor system.

The roll torques shown in figures 10 and 11 are not all-inclusive. They are only the incremental stochastic disturbance components. Within the rotor model, these increments are added to the large cyclic velocities of the individual blade elements, which become more pronounced with increased vehicle velocity. These total

element velocities are then used in aerodynamic look-up tables. Airspeed variations on advancing and retreating blades are thus computed using DOBEST in a distributed rotor model.

FREQUENCY FOLDING

As the blades track each other in a rotor system, an important phenomenon occurs. The frequency at the rpm ($\Omega_T = 27$ rad/sec) folds to higher harmonics that are multiples of the number of blades. This occurs for summations of blade contributions, such as in the torque proportionality equation. It occurs because for periodic behavior such as flapping, the dynamics of a given blade are essentially those of another blade, shifted in time (or multiples of 90 degrees). This phenomenon was examined in reference 8.

The phenomenon, however, does not occur for the stochastic components of turbulence, and is not observed in figures 11b, 11d, and 11f, which represent vehicle torque contributions owing to stochastic turbulence. For stochastic turbulence, the reason why frequency folding under blade summation does not occur is that the velocities of the elements on a blade are not time-shifted replications of another blade. They are statistically correlated velocities *that occur at the same time*. This is illustrated in figure 12, where the vertical velocity histories of all four blades are given. The interval of time that is shown represents two complete rotor revolutions, and element velocities are displayed for the case of $h = 500$ ft and $V_{RW} = 200$ ft/sec. The inboard-element velocity appears at the top of each graph, and the outboard-element velocity is at the bottom.

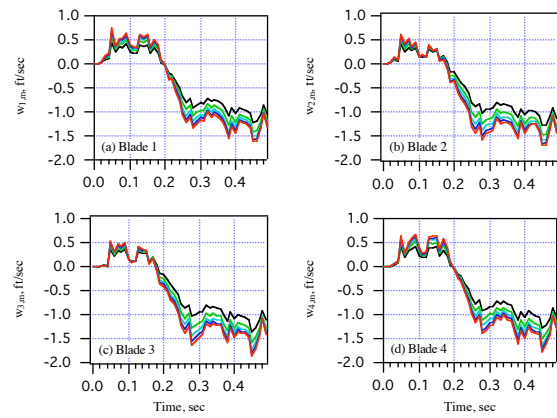


Figure 12. Blade vertical velocities.

It takes 0.0582 sec for a blade to travel 90 degrees. If this delay occurred between the velocities of blades that are separated by 90 degrees, it would be obvious in figure 12. Hence, as was shown in figures 11a, 11c, and 11e, there are no periodic components in the superimposed turbulence velocities of the DOBEST model. Thus, these velocities cannot contribute to the N/rev phenomenon when they are transformed and summed into the vehicle axes. This is verified by figures 11b, 11d, and 11f.

The 1/rev amplification for high-altitude flight, shown in figure 11f, is a result of the total roll torque summation, which has the one-per-rev frequency content when the blade velocities are highly correlated, but have (slightly) different magnitudes, as shown in figure 12.

Body-axis contributions (hub, tail) to turbulence have not been illustrated here, although the required random variables at the pertinent locations have been derived. These contributions utilize the vehicle velocity with respect to the mean wind in their filter representations. This velocity is typically lower-limited to about 10 ft/sec in discrete simulation. In hover, it is anticipated that body-axis contributions will be small compared to the rotor contributions, except for yaw disturbances. In testing the SORBET model of reference 3, pilots did not detect any improvement in yaw performance when tail rotor disturbances were added to the simulation (but SORBET did not feature the low hub-to-tail correlation developed here). Yaw activity is certain to increase with low correlation between hub and tail disturbances.

As shown in appendix B, the performance of the baseline model is not acceptable at any velocity condition except $V_{RW} = 0$, where it collapses to the DOBEST model. Fortunately, the workload of the DOBEST model is an order of magnitude less than that required for the "baseline" model.

CONCLUSIONS

A stochastic turbulence model, called DOBEST, has been developed for rotorcraft simulation. It represents a new approach to turbulence simulation and overcomes many of the difficulties associated with low aerodynamic velocities. In this model, turbulence is treated by superimposition, and Gaussian statistical properties are preserved through stationary atmospheric filters.

Random inputs from discrete noise sources are cyclically distributed to the locations of finite elements on the rotating blades. Rotor disturbances are then developed independent of periodic, asymmetric airspeeds at blade-element locations. This is accomplished by use of stationary filter coefficients that utilize an average aerodynamic velocity at each radial station. The algorithm thus avoids the intractable problem of cyclostationary turbulence filters. Body-axis disturbances are treated in the conventional fashion, except that turbulence is distributed to the aerodynamic centers of the model.

Spectral relationships are developed as functions of turbulence scale length in each dimension, and the reduction in correlation for low-altitude flight is shown to severely influence the vehicle's rotational responses.

The DOBEST model produces only stochastic turbulence. It may be used to augment discrete gust models, where inputs are from tables created by CFD analysis, as functions of location with respect to terrain or a ship, as in the JSHIP application. Terrain-correlated gust velocities, as well as pertinent energy variables, may be shared with DOBEST. Transfer function poles would be controlled by energy considerations of the gust model. The superimposition of random components of turbulence to gust models should add value to piloted simulation for low-speed and hovering operations around ships and other structures.

REFERENCES

1. Chalk, C. R.; Neal, T. P.; Harris, T. M.; and Pritchard, F. E.: Background Information and User Guide for MIL-F-8785B(ASG), Military Specification - Flying Qualities of Piloted Airplanes. AFFDL-TR-69-72, Air Force Flight Dynamics Laboratory, Wright Patterson AFB, Ohio, 1969.
2. Howlett, J. J.: UH-60A Black Hawk Engineering Simulation Program. Vol. 1, Mathematical Model. NASA CR-166309, Dec. 1981.
3. McFarland, R. E.; and Duisenberg, Ken: Simulation of Rotor Blade Element Turbulence. NASA TM-198862, Jan. 1995. (United States Patent No. 5,860,807, System and Method for Finite Element Simulation of Helicopter Turbulence, Jan. 19, 1999).
4. Sahasvabudhe, Vineet; Aponso, Bimal L.; Clement, Warren F.; and Jewell, Wayne F.: Terrain-Correlated Turbulence Models for Rotorcraft Nap-of-the-Earth Flight Simulations. NAS2-14105. Presented at the American Helicopter Society 55th Annual Forum, Montreal, Quebec, Canada, May 1999.
5. Military Specification, Flying Qualities of Piloted Airplanes. MIL-F-8785C superseding MIL-F-8785B of Aug. 7, 1969, dated Nov. 5, 1980.
6. McFarland, R. E.: Finite Element Aircraft Simulation of Turbulence. NASA TM-110437, Feb. 1997.
7. Military Standard, Flying Qualities of Piloted Aircraft. MIL-STD-1797A superseding MIL-STD-1797(USAF) of March 31, 1987, dated Jan. 30, 1990.
8. McFarland, R. E.: The N/Rev Phenomenon in Simulating a Blade-Element Rotor System. NASA TM-84344, Mar. 1983.
9. McFarland, R. E.: Quiet Mode for Nonlinear Rotor Models. NASA TM-102236, Apr. 1990.

APPENDIX A: FILTER VELOCITIES

For use in turbulence filter coefficients, blade-element velocities $V_{n,m}$ are developed in this appendix. These velocities include contributions from both the vehicle's aerodynamic velocity V_{RW} and the element's velocity due to blade rotation $\Omega_T r_m$. The approximation of the DOBEST model is then introduced, where the cyclostationary components of the element velocities are averaged over a rotor revolution, producing V_m .

Baseline Velocities

The total aerodynamic velocity of the vehicle V_{RW} may be represented in the rotor system's hub frame by

$$V_{RW} = \sqrt{V_x^2 + V_y^2 + V_z^2}$$

Because mast angles are typically small, the hub frame is nearly coincident with the vehicle frame. The aerodynamic velocity V_{RW} of the vehicle may be defined in terms of the angle of attack α and sideslip β with respect to the hub frame. The components of the aircraft's aerodynamic velocity are then given by

$$\begin{aligned} V_x &= V_{RW} \cos \beta \cos \alpha \\ V_y &= V_{RW} \sin \beta \cos \alpha \\ V_z &= V_{RW} \sin \alpha \end{aligned}$$

The hub frame is convenient for defining the total aerodynamic velocity of any element on any blade. The following parameters are used in this development.

$$\begin{aligned} a_m^2 &= \frac{2\Omega_T r_m V_{RW} \cos \alpha}{V_{RW}^2 + \Omega_T^2 r_m^2} \\ b_m^2 &= V_{RW}^2 + \Omega_T^2 r_m^2 \\ c_m &= b_m \sqrt{1 + a_m^2} \\ \kappa_m^2 &= \frac{2a_m^2}{1 + a_m^2} \\ \theta_n &= \psi_n + \beta \end{aligned}$$

Neglecting blade flapping and lagging, each element's velocity is a function of both its azimuth angle ψ_n and its radial position r_m :

$$\begin{aligned} V_{n,m} &= \sqrt{(V_x + \Omega_T r_m \sin \psi_n)^2 + (V_y + \Omega_T r_m \cos \psi_n)^2 + V_z^2} \\ &= \sqrt{V_{RW}^2 + \Omega_T^2 r_m^2} \sqrt{1 + \frac{2\Omega_T r_m V_{RW} \cos \alpha}{V_{RW}^2 + \Omega_T^2 r_m^2} \sin(\psi_n + \beta)} \\ &= b_m \sqrt{1 + a_m^2 \sin \theta_n} \end{aligned}$$

This element velocity is that which is used in turbulence filter coefficients for the baseline model (not in the DOBEST model). For the first blade ($n = 1$) at an airspeed of $V_{RW} = 200$ ft/sec, the element velocities $V_{1,m}$ are as shown in figure 13. Other blades have the same profile, shifted by multiples of $\pi/2$ in azimuth angle, or 0.0582 sec in time, when $\Omega_T = 27$ rad/sec.

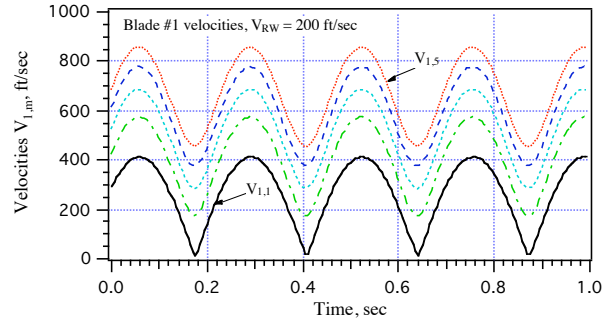


Figure 13. Velocities of elements, blade 1.

In figure 13 the inboard-element velocity $V_{1,1}$ is shown using a solid line and the outboard-element velocity is shown by a dotted line. The other element velocities are also shown.

For any vehicle velocity, the inequality $V_{n,m} \geq 0$ holds for all elements of all blades, so they may be used in the coefficients of the turbulence filters. For the baseline model this produces cyclostationary filters. The maximum and minimum values of the velocities used in the coefficients are given by

$$\begin{aligned} V_{n,m}(\max) &= \sqrt{V_{RW}^2 + \Omega_T^2 r_m^2 + 2\Omega_T r_m V_{RW} \cos \alpha} \\ V_{n,m}(\min) &= \sqrt{V_{RW}^2 + \Omega_T^2 r_m^2 - 2\Omega_T r_m V_{RW} \cos \alpha} \end{aligned}$$

For the case of $\alpha = 0$, these extrema reduce to

$$\begin{aligned} V_{n,m}(\max)_{\alpha=0} &= V_{RW} + \Omega_T r_m \\ V_{n,m}(\min)_{\alpha=0} &= |V_{RW} - \Omega_T r_m| \end{aligned}$$

(These are plotted as boundary limits in figures 16 and 17). The velocity $V_{n,m}$ vanishes periodically whenever $V_{RW} = \Omega_T r_m$.

As indicated in figure 13, all of the element velocities on a particular blade are in phase. The maximum values occur when $\sin \theta_n = 1$, and their magnitudes increase with segment number, m . The minimum values occur when $\sin \theta_n = -1$, and their magnitudes do not necessarily increase with segment number. For instance, the lowest

minimum value occurs for that element m which has a rotational velocity $\Omega_T r_m$ closest to the vehicle velocity V_{RW} . Mathematically, the crossover phenomenon begins to occur for an airspeed $V_{RW} > (r_1 + r_2) \Omega_T / 2$, which is 291.54 ft/sec. This velocity is beyond the operational capabilities of the Black Hawk.

The different blade velocities at a particular element radius r_m are out of phase by multiples of $\pi/2$. This is shown in figure 14, where just the inboard (first) element velocity is displayed, for all four blades, and at the same airspeed used in figure 13.

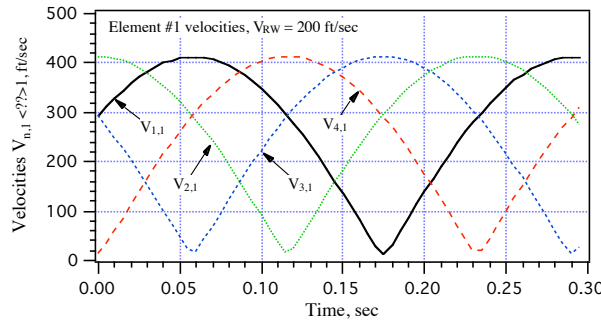


Figure 14. Velocities of blades, element 1.

In figures 13 and 14 the inboard element's radial velocity is very close to the vehicle velocity, and thus nearly vanishes periodically. Therefore, this element's pole ($p = V_{nm}/L$) in its turbulence filter also vanishes periodically. This phenomenon is particularly destructive, and will be shown to produce divergent responses. Element turbulence velocities generally become aberrant owing to these periodic velocities, as used by the baseline model.

DOBEST Velocities

In the DOBEST model, the average cyclostationary velocity of an element is used, where the average is obtained by integrating over the rotor plane azimuth angle θ_n . The average element velocity V_m (single subscript) at the radial station r_m is produced in the following derivation (θ_n becomes a dummy variable of integration):

$$\begin{aligned} V_m &= \frac{b_m}{2\pi} \int_0^{2\pi} \sqrt{1 + a_m^2 \sin^2 \theta_n} d\theta_n \\ &= \frac{2b_m}{\pi} \sqrt{1 + a_m^2} \int_0^{\pi} \sqrt{1 - \kappa_m^2 \sin^2 y} dy \\ &= b_m \sqrt{1 + a_m^2} [1 - S_m] = c_m [1 - S_m] \end{aligned}$$

In this equation,

$$\begin{aligned} \kappa_m^2 &= \frac{2a_m^2}{1 + a_m^2} \\ S_m &= \left(\frac{1}{2}\right)^2 \kappa_m^2 + \left(\frac{1}{2}\right)^2 \left(\frac{3}{4}\right)^2 \frac{\kappa_m^4}{3} + \left(\frac{1}{2}\right)^2 \left(\frac{3}{4}\right)^2 \left(\frac{5}{6}\right)^2 \frac{\kappa_m^6}{5} + \dots \\ &= \begin{cases} 0.25\kappa_m^2 + 0.046875\kappa_m^4 + 0.01953125\kappa_m^6 + \dots & \kappa_m^2 < 1 \\ 1 - \frac{2}{\pi} & \kappa_m^2 = 1 \end{cases} \end{aligned}$$

If coefficients ($j = 1, 2, 3, \dots, J$) are predefined,

$$R_j = \frac{1}{2j-1} \prod_{i=1}^j \left(1 - \frac{1}{2i}\right)^2$$

the real-time workload consists of only the J combinations,

$$S_m = \begin{cases} \sum_{j=1}^J \kappa_m^{2j} R_j & \kappa_m^2 < 1 \\ 1 - \frac{2}{\pi} & \kappa_m^2 = 1 \end{cases}$$

A value of about $J = 10$ is suggested for the series because it converges rather slowly as κ_m approaches unity. For a few high values of κ_m the convergence is illustrated in figure 15. The value for $\kappa_m = 1$ is also shown by the dotted line.

The series representation is applicable only for $\kappa_m < 1$. The variable κ_m is unity only if $\alpha = 0$ and $V_{RW} = \Omega_T r_m$, and if this occurs the closed form representation is used. If $V_{RW} = 0$, $\kappa_m = 0$ also, and the average element velocity is at its minimum value $V_m = \Omega_T r_m$. As indicated in figure 15, accurate values for the average velocity are produced by taking only a few terms in the series ($J = 10$).

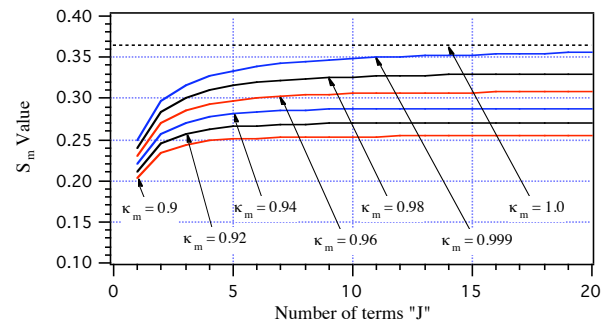


Figure 15. Convergence of summation

In contrast to figures 13 and 14, the resultant, average element velocities are independent of the azimuth angle. They are functions of the vehicle airspeed, the element radii, and the rotor system's angle of attack. The average velocity values are *not* the average values of the extrema of $V_{n,m}$. Element 1 is the inboard element on a blade, and its rotational velocity is smaller than that of any other element. Hence, its boundaries are the smallest for any airspeed.

The extreme element velocities, as well as the average element velocities, are as shown in figure 16 for the case of $\alpha = 0$. This figure takes great liberties with the operational velocity capability of the Black Hawk, which is less than 300 ft/sec. It is presented from a mathematical point of view only, in order to display the limits and averages, as V_{RW} approaches $\Omega_T r_m$. A compilation of the average element velocities is presented in figure 16f.

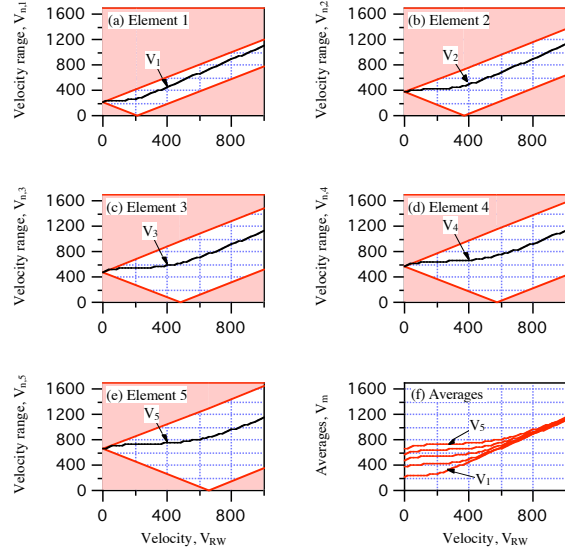


Figure 16. Velocity limits.

Using the operational velocity range for the Black Hawk, only the inboard element actually experiences the reverse-flow phenomenon. This is shown in figure 17a. The average velocities of the elements are different, but they vary little with airspeed from their values at $V_{RW} = 0$. This is seen in figure 17f. Hence, turbulence responses using the DOBEST model display very little dependence on airspeed. This phenomenon is examined in appendix B.

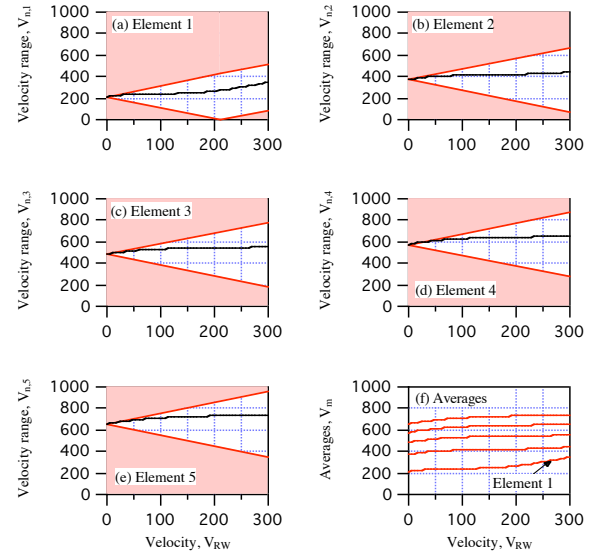


Figure 17. Velocity limits for the Black Hawk.

The extremes in average velocity are shown in table 3, where it is assumed that $V_{RW}(\max) = 300$ ft/sec. Only the inboard element shows a variation greater than 20%. Hence, as a function of airspeed, the filter poles ($p = V_m/L$) can only vary by this percentage in the DOBEST model.

Table 3. Average velocity limits.

Element	V_m (min)	V_m (max)	Range
1	212.25	348.70	64.3%
2	370.85	442.2	19.2%
3	482.83	553.21	14.6%
4	574.54	651.36	13.9%
5	654.14	738.12	12.8%

A feasible turbulence model for a rotor system could thus ignore airspeed variations. This "leap of faith," however, is not utilized in the DOBEST model developed herein.

At $V_{RW} = 0$ the turbulence ($u_{n,m}, v_{n,m}, w_{n,m}$) owing to using the baseline velocity $V_{n,m}$ is identical to that using the average velocity V_m , because all cyclostationary contributions vanish ($V_{n,m} = V_m$). Differences in turbulence between the baseline and DOBEST models occur only for $V_{RW} \neq 0$. These differences are discussed in appendix B.

APPENDIX B: TURBULENCE RESPONSES

For both the baseline and DOBEST models, filter responses to random variable time histories are examined in this appendix. The baseline responses are shown to deliver outputs that tend to diverge if an element's tangential velocity periodically approaches that of the vehicle's airspeed. Periodic filter coefficients produce unequal dispersions for each element, and they are functions of both airspeed and altitude. This presents an intractable modeling problem, and meaningful metrics for turbulence energy cannot be established.

Using the average element velocities of the DOBEST model, however, stationary filters are implemented at each element location, and, in response to random variables, their outputs deliver the correct dispersions, independent of airspeed and altitude.

The turbulence trends for most elements have similarities for both models, except that the DOBEST model does not display the divergent element velocities of the baseline model, and energy metrics are retained.

It is also shown that in the DOBEST model, vehicle airspeed has little influence on filter outputs. An element's rotational velocity component overwhelms airspeed influences to such an extent that airspeed may itself be ignored. This further simplification could be used to advantage because it vastly simplifies computations.

The vertical turbulence velocity w_{nm} presents the greatest challenge in discrete computation, because the filter pole range is largest. This occurs because the scale length is smallest ($h = L_w \leq L$), and the pole in the vertical filter for an element is given by $p = V_{nm}/L_w$. As previously determined, the turbulence scale length L_w is restricted to a minimum of 26.2 ft (at $V_{RW} = 0$), despite the fact that altitude may be lower. For the baseline model, although this produces relatively large poles, they may also periodically vanish. This phenomenon cannot occur in the DOBEST model.

The very low altitude of $h = 10$ ft is selected in the first sample for display, and it produces the largest system poles. Then the same display is given for the case of $h = 500$ ft, such that the system poles are reduced by an order of magnitude. Turbulent velocities versus time are displayed for 5 sec in these examples. The input dispersion used is $\sigma_w = 1$ ft/sec. Both the baseline model and the DOBEST model are shown at four different airspeeds. All five of the vertical element velocities are given on each graph in figure 18, for one blade. The proximity of an element's tangential velocity to the airspeed produces the aberrant behavior.

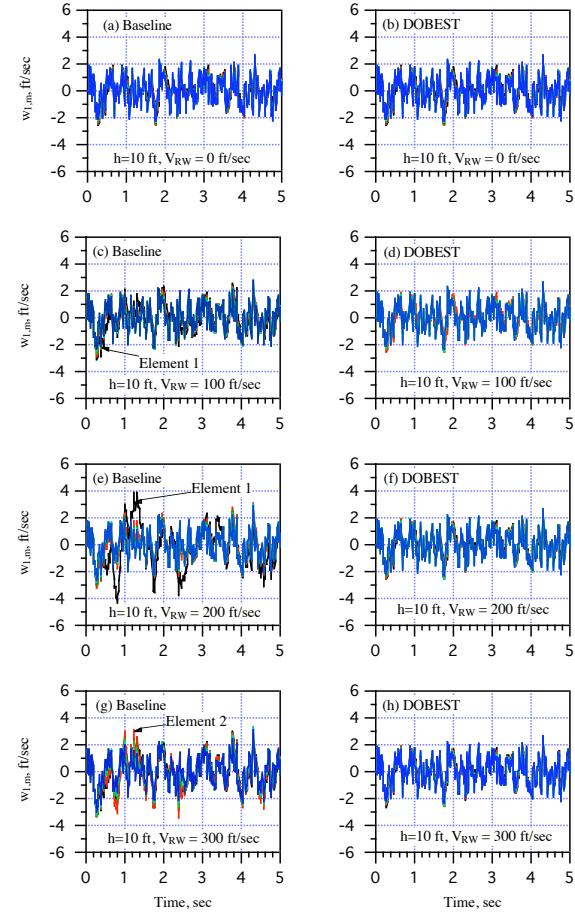


Figure 18. Element velocities, $h = 10$ ft.

From table 1, these tangential components were given as 212 and 371 ft/sec for elements 1 and 2, respectively. When V_{RW} is 200 ft/sec, as in figure 18e, the response of element 1 is aberrant. When it is 300 ft/sec, as in figure 18f, element 2 becomes aberrant. These aberrations are not dramatic for this case of $h = 10$ ft as is the case where $h = 500$ ft, because the poles are generally large, and rarely in their periodic, near-vanishing region.

Statistically, significant differences nonetheless occur between the baseline and DOBEST models. The DOBEST model delivers the input unity dispersion, but the baseline model delivers dispersions that are a function of vehicle velocity, as well as element radius. The baseline model delivers the dispersions shown in figure 19. Dispersion were computed as a function of airspeed every 20 ft/sec, to a maximum of 1,000 ft/sec. Although this final airspeed is well over three times the operational capacity of the Black Hawk, these curves are presented

only to illustrate the uniform degradation in turbulence metrics as the vehicle airspeed approaches that of any given element.

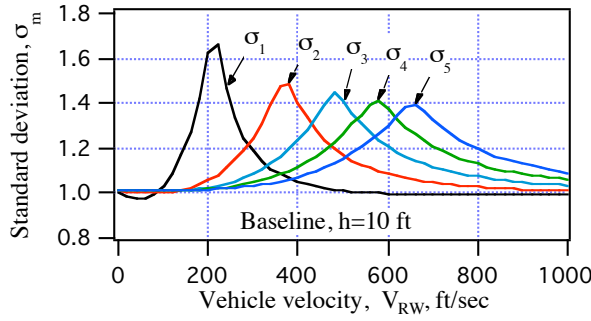


Figure 19. Baseline, $h = 10$ ft.

The maxima of these curves occur at $V_{RW} = \Omega_T r_m$. The maxima decrease with element number because the radial velocity increases with element number, that is, the higher the radial velocity, the less time the element's velocity spends around its lowest value.

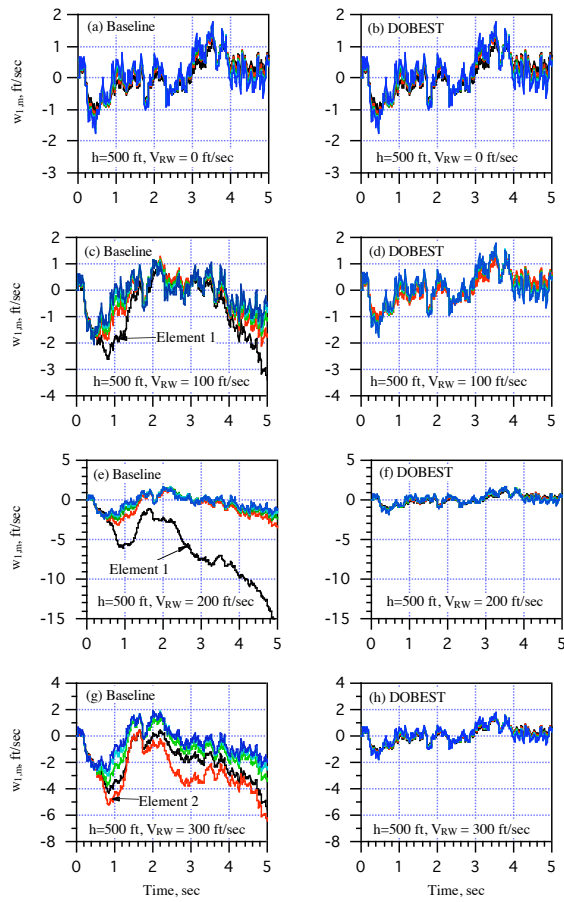


Figure 20. Element velocities, $h = 500$ ft.

The cases in which $h = 500$ ft are much more illustrative. The poles are an order of magnitude smaller than those used in the previous graphs, so the aberrations are much more pronounced. In figure 20e only the inboard element (No. 1) actually diverges in the displayed time interval. This occurs because $\Omega_T r_1$ approaches $V_{RW} = 200$ ft/sec. In figure 20g both elements 1 and 2 begin to diverge.

For the high-altitude cases of figure 20, the DOBEST model again delivers the input unity dispersion, but the baseline model fails to establish a meaningful energy metric. These data are shown in figure 21, where the dispersions should all be unity for all airspeeds. Once more, the graph takes great liberties with the operational capabilities of the Black Hawk. The errors are quite large in the operational velocity region below 300 ft/sec. These errors are further increased for higher altitude flight, because the filter's poles become correspondingly smaller.

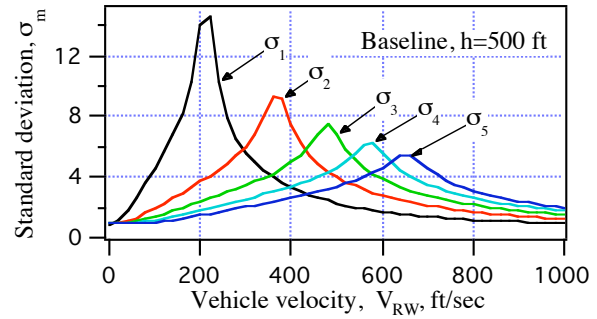


Figure 21. Baseline, $h = 500$ ft.

In comparing the baseline and DOBEST models, it is also of interest to look at all four blades at a specific flight condition. The parameters $V_{RW} = 200$ ft/sec and $h = 500$ ft were used to create the next two sets of graphs. In figure 22 it is seen that the trend of element velocities in the baseline model is random, and they quickly diverge. These velocities are nonsensical. They cannot be superimposed on the other components of blade-element velocities in a rotor model because they would rapidly crash the vehicle.

Because of the airspeed, the most divergent trace in figure 22 is for the inboard element. For the DOBEST model, the same parameters are used; the responses are given in figure 23. Note that the velocities are quite similar for all segments, and for all blades.

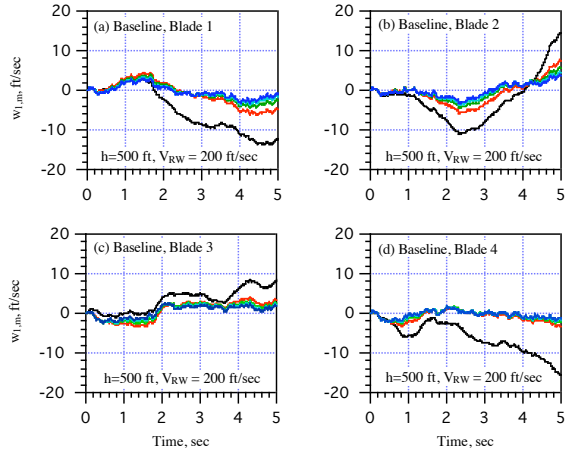


Figure 22. Baseline blade responses.

Identical random noise inputs were used to create all of the graphs in this appendix. Hence, figure 20e and figure 22d display the same data, using different scales. The same is true for figure 20f and figure 23d.

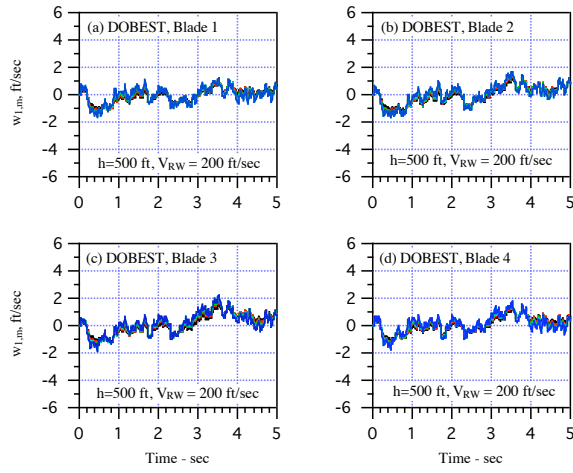


Figure 23. DOBEST blade responses.

The DOBEST model's outputs are relatively insensitive to vehicle velocity. This is seen in a comparison of figures 20b-20f and 20h. The filter pole, however, is inversely proportional to the characteristic length of turbulence, such that filter outputs are sensitive to altitude variations. From the DOBEST model, this is shown in figure 24, for three different altitudes and two different velocities.

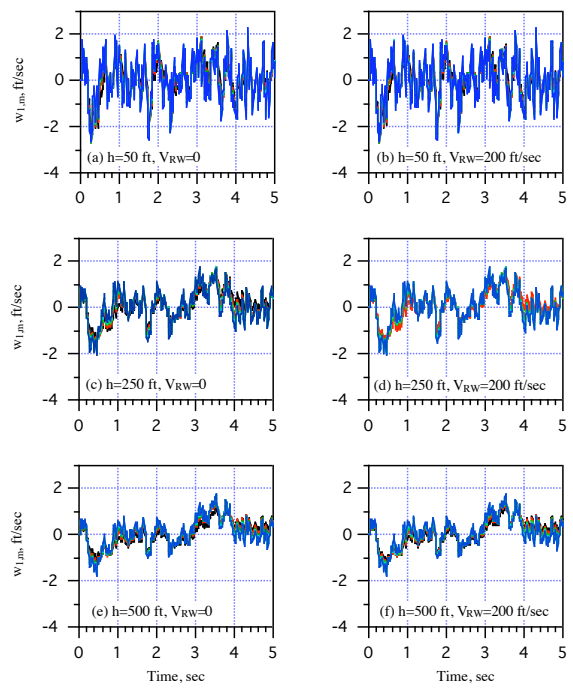


Figure 24. DOBEST comparisons.

A comparison of the set of graphs in figure 24, by looking in the vertical dimension, shows that variations in altitude indeed alter the turbulence histories. The poles vary considerably with altitude because of the inverse relationship.

However, a comparison of these graphs by looking in the horizontal dimension shows small differences. The distributed random inputs dominate the responses. Defining the filter poles as functions of element rotational velocity appears to produce a feasible model. Since the computation of the average velocity per element (see appendix A) has little influence on the results, the use of $V_{RW} = 0$ in the rotor computations is probably sufficient for most applications. Nonetheless, the airspeed contribution is retained in the DOBEST model.

APPENDIX C: REAL-TIME COMPUTATION

The real-time workload is presented in this appendix for the DOBEST model. The workload for the baseline model is similar, but much more complicated because each and every element has its own unique filter coefficients at each instant of time. The workload is divided into two parts, where the first part consists of computations for slowly varying quantities. The computational workload of these equations may be segmented such that it is divided over a number of cycles. This is not true for the baseline model. The second part consists of computations that must be performed on each computer cycle.

Slowly Varying Functions

Slowly varying quantities are computed as a function of altitude and vehicle velocity:

$$f_h = 0.177 + 0.000823h$$

$$L = \begin{cases} 75.64 & h \leq 10 \\ hf_h^{-1.2} & 10 < h \leq 1000 \\ h & 1000 < h \leq 1750 \\ 1750 & h \geq 1750 \end{cases}$$

$$L'_w = \begin{cases} 10 & h \leq 10 \\ h & 10 < h \leq 1750 \\ 1750 & h > 1750 \end{cases}$$

$$L_w = \begin{cases} 26.2 & h \leq 26.2 \\ L'_w & h > 26.2 \end{cases}$$

$$\sigma = \begin{cases} \sigma_w f_h^{-0.4} & h < 1000 \\ \sigma_w & h \geq 1000 \end{cases}$$

After the above computations, the vertical scale lengths are further restricted by functions of airspeed:

$$L'_w = \begin{cases} L'_w & L'_w \geq V_{RW}/25 \\ V_{RW}/25 & \text{otherwise} \end{cases}$$

$$L_w = \begin{cases} L_w & L_w \geq 26.2 + V_{RW}/25 \\ 26.2 + V_{RW}/25 & \text{otherwise} \end{cases}$$

Parameters pertinent to body-axis turbulence are:

$$V'_{RW} = \begin{cases} 10 & V_{RW} \leq 10 \\ V_{RW} & V_{RW} > 10 \end{cases}$$

$$\beta = \frac{V'_{RW}\Delta t}{L'_w}$$

$$G = \sigma \sqrt{\frac{2}{\beta}} (1 - e^{-\beta})$$

$$\alpha'' = \frac{V'_{RW}\Delta t}{L}$$

$$D'' = \sigma \sqrt{\frac{1}{\alpha''}} \left[1 - e^{-\alpha''} + (\sqrt{3} - 1) \alpha'' e^{-\alpha''} \right]$$

$$E'' = \sigma \sqrt{\frac{1}{\alpha''}} \left[e^{-\alpha''} - 1 - (\sqrt{3} - 1) \alpha'' \right] e^{-\alpha''}$$

$$D''' = \sigma_w \sqrt{\frac{1}{\beta}} \left[1 - e^{-\beta} + (\sqrt{3} - 1) \beta e^{-\beta} \right]$$

$$E''' = \sigma_w \sqrt{\frac{1}{\beta}} \left[e^{-\beta} - 1 - (\sqrt{3} - 1) \beta \right] e^{-\beta}$$

These coefficients for body-axis turbulence are identical to those used by models for conventional aircraft.

Parameters required for tail turbulence are:

$$d_T = \frac{2r_G}{L}$$

$$\rho_T = (1 - d_T) e^{-d_T}$$

$$A_T = \frac{1}{2} \left(\sqrt{1 + \rho_T} + \sqrt{1 - \rho_T} \right)$$

$$B_T = \frac{1}{2} \left(\sqrt{1 + \rho_T} - \sqrt{1 - \rho_T} \right)$$

For rotor turbulence, where $m = 1, 2, 3, 4, 5$, parameters pertinent to the blade elements are

$$d_m = \frac{2r_m}{L}$$

$$\rho_m = (1 - d_m) e^{-d_m}$$

$$A_m = \frac{1}{2} \left(\sqrt{1 + \rho_m} + \sqrt{1 - \rho_m} \right)$$

$$B_m = \frac{1}{2} \left(\sqrt{1 + \rho_m} - \sqrt{1 - \rho_m} \right)$$

Five matrices of coefficients are produced from the above computations:

$$[M]_m = \begin{bmatrix} 0 & 0 & 0 & 0 & A_0 & B_0 \\ A_m & 0 & B_m & 0 & 0 & 0 \\ 0 & A_m & 0 & B_m & 0 & 0 \\ B_m & 0 & A_m & 0 & 0 & 0 \\ 0 & B_m & 0 & A_m & 0 & 0 \\ 0 & 0 & 0 & 0 & A_T & B_T \end{bmatrix}$$

Since five blade-element radii are considered, five sets of coefficients are required for their turbulence filters (see appendix A, especially for the additional considerations required in the baseline model):

$$V_m = (1 - S_m) \sqrt{V_{RW}^2 + \Omega_T^2 r_m^2 + 2\Omega_T r_m \cos\alpha}$$

$$\alpha_m = \frac{V_m \Delta t}{L}$$

$$\alpha'_m = \frac{V_m \Delta t}{L_w}$$

$$D_m = \sigma \sqrt{\frac{1}{\alpha_m}} \left[1 - e^{-\alpha_m} + (\sqrt{3} - 1) \alpha_m e^{-\alpha_m} \right]$$

$$E_m = \sigma \sqrt{\frac{1}{\alpha_m}} \left[e^{-\alpha_m} - 1 - (\sqrt{3} - 1) \alpha_m \right] e^{-\alpha_m}$$

$$D'_m = \sigma_w \sqrt{\frac{1}{\alpha'_m}} \left[1 - e^{-\alpha'_m} + (\sqrt{3} - 1) \alpha'_m e^{-\alpha'_m} \right]$$

$$E'_m = \sigma_w \sqrt{\frac{1}{\alpha'_m}} \left[e^{-\alpha'_m} - 1 - (\sqrt{3} - 1) \alpha'_m \right] e^{-\alpha'_m}$$

$$\begin{bmatrix} \mu_1 \\ \mu_2 \\ \mu_3 \\ \mu_4 \\ \mu_5 \\ \mu_6 \end{bmatrix}_k = [T] \begin{bmatrix} \varepsilon_1 \\ \varepsilon_2 \\ \varepsilon_3 \\ \varepsilon_4 \end{bmatrix}_k$$

From the matrices of coefficients, 22 inputs are created per axis:

$$\begin{bmatrix} \eta_0 \\ \eta_{1,m} \\ \eta_{2,m} \\ \eta_{3,m} \\ \eta_{4,m} \\ \eta_5 \end{bmatrix}_k = [M]_m \begin{bmatrix} \mu_1 \\ \mu_2 \\ \mu_3 \\ \mu_4 \\ \mu_5 \\ \mu_6 \end{bmatrix}_k$$

At the center of mass (variable 0) the filter solutions for the three vehicle axes are given by the difference equations,

$$\begin{aligned} u_{0,i} &= e^{-\beta} u_{0,i-1} + G \eta_{0,1,i} \\ v_{0,i} &= 2e^{-\alpha''} v_{0,i-1} - e^{-2\alpha''} v_{0,i-2} + D'' \eta_{0,2,i} + E'' \eta_{0,3,i-1} \\ w_{0,i} &= 2e^{-\beta} w_{0,i-1} - e^{-2\beta} w_{0,i-2} + D''' \eta_{0,3,i} + E''' \eta_{0,3,i-1} \end{aligned}$$

These translational turbulence equations are the same as those used in conventional aircraft applications for the center of mass.

For the distributed system the tail contribution (variable 5) is also included:

$$\begin{aligned} u_{5,i} &= e^{-\beta} u_{5,i-1} + G \eta_{5,1,i} \\ v_{5,i} &= 2e^{-\alpha''} v_{5,i-1} - e^{-2\alpha''} v_{5,i-2} + D'' \eta_{5,2,i} + E'' \eta_{5,2,i-1} \\ w_{5,i} &= 2e^{-\beta} w_{5,i-1} - e^{-2\beta} w_{5,i-2} + D''' \eta_{5,3,i} + E''' \eta_{5,3,i-1} \end{aligned}$$

Note that the longitudinal body filters use the first-order filters derived from table 2. All body-axis filters thus conform to models for conventional aircraft.

For each blade element, of which there are 20, the three components of turbulence velocity are given by the difference equations,

$$\begin{aligned} u_{n,m,j} &= 2e^{-\alpha_n} u_{n,m,j-1} - e^{-2\alpha_n} u_{n,m,j-2} + D_m \eta_{n,m,1,j} + E_m \eta_{n,m,1,j-1} \\ v_{n,m,j} &= 2e^{-\alpha_n} v_{n,m,j-1} - e^{-2\alpha_n} v_{n,m,j-2} + D_m \eta_{n,m,2,j} + E_m \eta_{n,m,2,j-1} \\ w_{n,m,j} &= 2e^{-\alpha_n'} w_{n,m,j-1} - e^{-2\alpha_n'} w_{n,m,j-2} + D'_m \eta_{n,m,3,j} + E'_m \eta_{n,m,3,j-1} \end{aligned}$$

Considering all three vehicle axes, 60 velocity components are computed at the pertinent blade-element locations, and are summed with the other velocity components of the rotor model.

For each cycle time the rotation matrix is

$$[T] = \frac{1}{\sqrt{8}} \begin{bmatrix} 1 + \sqrt{2}C & 1 + \sqrt{2}S & 1 - \sqrt{2}C & 1 - \sqrt{2}S \\ 1 - \sqrt{2}S & 1 + \sqrt{2}C & 1 + \sqrt{2}S & 1 - \sqrt{2}C \\ 1 - \sqrt{2}C & 1 - \sqrt{2}S & 1 + \sqrt{2}C & 1 + \sqrt{2}S \\ 1 + \sqrt{2}S & 1 - \sqrt{2}C & 1 - \sqrt{2}S & 1 + \sqrt{2}C \\ 1 + \sqrt{2} & 1 & 1 - \sqrt{2} & 1 \\ 1 - \sqrt{2} & 1 & 1 + \sqrt{2} & 1 \end{bmatrix}$$

Twelve random variables are acquired in three sets, $(\varepsilon_1, \varepsilon_2, \varepsilon_3, \varepsilon_4)_k$, where the axis identifier is $k = 1, 2, 3$. Six random variables per axis are computed: